


Online Feedback Optimization for Emergency Power System Operation

Master Thesis

Author(s):

Hotz, Gianni 

Publication date:

2021-11-01

Permanent link:

<https://doi.org/10.3929/ethz-b-000518176>

Rights / license:

In Copyright - Non-Commercial Use Permitted



Eidgenössische Technische Hochschule Zürich
Swiss Federal Institute of Technology Zurich



Automatic Control Laboratory

Master's Thesis
Online Feedback Optimization for Emergency
Power System Operation

Gianni Hotz
November 1, 2021

Advisors

Lukas Ortmann, Saverio Bolognani, Florian Dörfler

Abstract

With increasing intermittent distributed power generation, emergency situations in the power system are more likely to occur. Current emergency operation in power systems is mostly based on manual remedial actions. The growing number of distributed generation devices add complexity to emergency operation and make decisions on remedial actions harder. In this thesis, a feedback optimization (FO) controller for emergency power system operation is implemented. To reflect the fast timescales and model inaccuracies in emergency operation, FO is pushed beyond the limit of current stability and robustness methods. As a benchmark for the FO controller, a controller based on the optimal power flow (OPF) approach is used. Both controllers are tested using the dynamic power system simulator DynPSSimPy. In contrast to the OPF controller, the FO controller meets all the posed operational constraints, even in the presence of imperfect model information. In terms of optimality, imperfect model information can cause both controllers to converge to a suboptimal operating point. Based on timescale separation, two methods of estimating the step size limit and thus guarantee convergence of the FO controller are applied. No practical relevant certificates for the stability and robustness of the FO controller can be made, since the step size limit estimations yield either too high, or too conservative limits. However, the simulations show evidence, that FO is applicable to emergency power system operation by controlling the system stably even in the presence of imperfect model information. With that, FO is capable of supporting power system operators in handling complex emergency situations.

Preface

I chose this thesis to combine my interests in power systems with those of control theory. Working on this project not only allowed me to apply knowledge in the fields of power systems and control theory, but a variety of skills acquired during the last years of studying. With this thesis, my studies at ETH Zurich come to an end. I look back to a great and very instructive time, and look forward to future challenges in my professional life. I am grateful for the opportunity of completing my degree at ETH Zurich and want to thank everyone who contributed to this. I want to express my particular gratitude to the supervisors of this thesis, Lukas Ortmann and Dr. Saverio Bolognani, for the valuable discussions and their support during the thesis. Further, I'd like to thank Keith Moffat from UC Berkley for the interesting inputs to this thesis during his visit at ETH Zurich and Hallvar Haugdal from NTNU for helping me with the dynamic system simulator used in this work. Finally, my thanks go to Prof. Dr. Florian Dörfler for providing me the opportunity of this thesis.

Contents

List of Figures	ix
List of Tables	xi
1 Introduction	1
2 Power System Modelling	3
2.1 Power System Admittance Matrix	3
2.2 Static Power Flow Solution	4
2.2.1 Modelling of Distributed Slack	5
2.3 Dynamic Power System Model	7
2.3.1 Synchronous Machine	7
2.3.2 Automated Generation Control	12
2.4 Review on Dynamic Power System Simulators	12
3 Feedback Optimization for Emergency Operation	15
3.1 Review of Feedback Optimization	15
3.1.1 Projected Gradient Descent Flow	16
3.2 Controlling a Power System with Feedback Optimization	18
3.2.1 Computation of Sensitivities	19
3.3 Tuning of the Feedback Optimization Controller	21
3.3.1 Timescale Separation through Step Size Limit	21
4 Simulation Environment & Results	25
4.1 Simulation Environment	25
4.1.1 Feedback Optimization Controller	25
4.1.2 Optimal Power Flow Controller as a Benchmark	27
4.2 Simulation Results	28
4.2.1 Working Principles of Controllers	28
4.2.2 Control in Emergency Operation	31
4.2.3 Stability of Feedback Optimization Controller	32
4.2.4 Robustness of Feedback Optimization Controller	36
5 Conclusion	39
A Technical Data IEEE 39 Bus System	41
Bibliography	47

List of Figures

2.1	Block diagram of governor model <i>TGOV1</i>	10
2.2	Block diagram of the excitation system model <i>SEXS</i>	10
2.3	Block diagram of the power system stabilizer <i>STAB1</i>	11
2.4	Block diagram of the automated generation control.	12
3.1	Block diagram of the dynamic power system simulator <i>DynPSSimPy</i> including the FO controller. The blocks PSS, AVR, GOV, GEN, AGC, PF and FO correspond to the power system stabilizer, the automated voltage regulator, the governor, the synchronous machine, the excitation system, the power flow equations and the FO controller, respectively. The blocks corresponding to one generating unit are grouped by the dotted frame, and possible additional generation units are indicated by the second dotted frame.	20
4.1	Single line diagram of IEEE 39 bus system [32]. Generator 1, located at bus 39 at the very left of the diagram (this bus and generator are not labelled in the figure), represents an aggregation of a bigger power system with multiple generators.	26
4.2	Objective function value of the economic dispatch simulation for the FO and OPF controllers, the uncontrolled system and the steady state optimum. The vertical blue line marks the starting point of the controllers.	29
4.3	Upper panel: Active power generation set point during the first seconds of the economic dispatch simulation with the FO controller. The vertical red line shows the operating limit. Lower panel: Generator speed during the first seconds of the economic dispatch simulation with the FO controller. The orange line depicts the average system frequency $\bar{\omega}$	29
4.4	Input and output variables of the power system in the economic dispatch simulation for the FO and OPF controllers, with their constraints indicated by the horizontal red lines. The vertical blue line marks the starting point of the controllers.	30
4.5	Voltage difference of buses B23 and B24 in the emergency operation simulation for the FO and OPF controllers, the uncontrolled system and the steady state optimum. The vertical blue lines mark the disconnection of line L23-24, the starting point of the controllers and the reclosure of line L23-24, respectively.	32
4.6	Input and output variables of the power system in the emergency operation simulation for the FO and OPF controllers, with their constraints indicated by the horizontal red lines. The vertical blue lines mark the disconnection of line L23-24, the starting point of the controllers and the reclosure of line L23-24, respectively.	33
4.7	Branch currents magnitudes in the emergency operation simulation. Line L23-24 is highlighted in orange. The vertical blue lines mark the disconnection of line L23-24, the starting point of the controllers and the reclosure of line L23-24, respectively.	34

4.8	Step size limit estimate $\hat{\alpha}_{max}$ in the emergency operation set-up. The straight black and dark grey lines show the estimates based on the set of random states and inputs, while the light grey line shows how the step size limit estimate changes based on the operating points of the emergency operation simulation. The vertical blue lines mark the disconnection of line L23-24, the starting point of the controller and the reclosure of line L23-24, respectively.	35
4.9	Voltage differences of buses B23 and B24 in the emergency operation simulations for the FO controller with different sensitivities. The simulation with the actual sensitivities is highlighted in orange. The vertical blue lines mark the disconnection of line L23-24, the starting point of the controller and the reclosure of line L23-24, respectively.	37

List of Tables

2.1	Parameters of the synchronous machine model [7].	9
2.2	Parameters of the governor model [20].	9
2.3	Parameters of the excitation system model [20].	11
2.4	Parameters of the power system stabilizer model.	11
2.5	Parameters of the automated generation control model [7].	12
2.6	Comparison of dynamic power system simulators.	13
4.1	Step size limit estimates $\hat{\alpha}_{max}$ computed with the parameter fitting and linearization method based on random operating points and with the linearization method based on the operating points of the emergency operation example.	34
4.2	Convergence test for the emergency operation simulation with different step sizes α and sampling times of the FO controller τ_{FO} . α_{lim} represents the maximum step size at the given sampling time for which the system converges in this set-up. * Theoretic convergence.	36
A.1	Technical data of the transformers in the IEEE 39 bus system: transformer resistance r_{ij} and reactance x_{ij} and the voltage ratios t_{ij} and t_{ji}	41
A.2	Overview of the buses in the IEEE 39 bus system: Bus nominal voltage $v_{n,i}$, bus type, active and reactive load power withdrawal $p_{L,i}$ and $q_{L,i}$, respectively.	42
A.3	Technical data of the lines in the IEEE 39 bus system: line resistance r_{ij} and reactance x_{ij} and the shunt susceptance of the line b_{ij}^{sh} along with the line length.	43
A.4	Technical data of the synchronous machines in the IEEE 39 bus system as described in table 2.1 and the power rating of the synchronous machines S_i . The armature winding resistance of the synchronous machines is neglected in the used simulation set-ups.	44
A.5	Technical data of the governors in the IEEE 39 bus system, as described in table 2.2.	45
A.6	Technical data of the excitation systems in the IEEE 39 bus system, as described in table 2.3.	45
A.7	Technical data of the power system stabilizers in the IEEE 39 bus system, as described in table 2.4.	45

Chapter 1

Introduction

Decarbonizing the electric power generation leads to increasing penetration of fluctuating and distributed renewable energy generation [1]. This poses new challenges to the electric power system. On transmission level, the intermittent and traditionally uncontrolled distributed power generation leads to distortions of the consumption patterns and hence increases the risk of unpredictable power flows, which can lead to highly loaded transmission elements (see [2] for an example). On distribution level, distributed energy generation leads to significant changes in the power flow direction. Traditional distribution systems are designed to supply consumers uni-directionally with electrical energy. Because of this approach, often no control of the system and therefore no accurate system models were needed [3]. With distributed energy sources, it is more necessary to control distributed generation devices in an ideally model-free way, because of the lack of accurate system models.

The power system state is categorized in four operation modes [4]. Normal operation mode is achieved when no contingency is causing any overload or other operating limit violation. Alert mode is reached, when either contingencies are causing the violation of operating limits, or certain operating limits are violated already slightly. Emergency operation mode requires the system operator to take immediate actions in order to prevent the shutdown of equipment and partial or complete blackouts. Restoration mode means that equipment that has been shutdown or parts of the power system that were disconnected are brought back online or connected to the power system.

Recent power system blackouts were mainly caused by network transmission equipment tripping [5]. Disconnecting these elements is often triggered by faults introduced by weather conditions or overloading of the equipment. The tripping of a highly loaded network element can result in cascading effects such as tripping of further transmission equipment or generators, frequency deviations, voltage collapse, and/or low-frequency oscillations [5]. These incidences can lead to partial or complete blackouts. Emergency operation tries to prevent the unintended shutdown of any power system element and the disconnection of any load.

Partially current emergency operation is done by automated controllers. The last attempt to stabilize the power system is when *special protection schemes* (SPS) are triggered. SPS are local controllers designed to prevent or minimize the impact of a power system collapse by recognizing specific network events (e.g., tripping of one specific line or generation unit) and taking predefined actions [6]. Examples for SPS are *under frequency load shedding* (UFLS), which disconnects loads in the power system in case of low frequency in order to restore the system frequency, or schemes, which reduce the generation power at specific generation units in case of a line disconnection. Although these protection schemes are an important part of the current power system emergency operation control, they are not of primary interest in this thesis, since they act as supplement to emergency operation in situations, that require a specific predefined action.

To prevent more general events like for instance tripping of transmission equipment or the

system voltage from collapsing, active and reactive power generation need to be adjusted. Similarly, severe frequency deviations can be corrected by activating tertiary frequency control [7]. These actions currently are taken manually by system operators. As in these examples, current emergency operation often requires manual actions. Due to the fast timescales of cascading effects, these actions are highly time-sensitive. Operators need to analyze the situation quickly and decide on appropriate actions to stabilize the power system. Usually, power system operators have tools such as power system simulators to support their decision. However, human operators often decide on remedial actions based on their experience. Possible reasons for this could be situations, where fast actions are required and there is no sufficient time to run simulations, or power system models of the simulation not representing the current emergency situation, leading to inappropriate simulation results. With the added complexity due to an increasing number of distributed generation and thus possibly controllable devices, manual and experience based decisions will become harder. A controller, which is robust against model uncertainties and capable of acting fast enough on the power system, clearly would be superior to the current emergency operation procedures.

Computational optimization is a common solution to finding the best option w.r.t. some criterion in complex systems. It has been a topic in power system operation since the 1960s (see review in [8]). Classical approaches try to minimize a cost function (e.g., power generation cost, losses, etc.) by finding the minimizing operating point of a power system offline. Therefore, an optimization problem with constraints given by a power system model is solved. Once the optimal operating point is known, the set points of the controllable devices in the power system are set according to the optimizing argument of the optimization problem to try to reach the optimal operating point of the power system in a feed-forward way. This approach is known as *optimal power flow* (OPF) [4]. Recently, *feedback optimization* (FO) has been applied to optimize power system operations [9–11]. Instead of using a model of the power system, FO uses measurements and iteratively drives the system to an operating point minimizing the considered cost function. In contrast to OPF, no model of the power system is needed. The sensitivities of how the system variables change after changing the set point of a controllable device are enough to steer the system to the optimal operating point. Additionally, the feedback used in the FO approach has the advantages of making it more robust against inaccurate power system models and disturbances. These two properties reduce the model-dependence of FO. Furthermore, computational effort is reduced, because the power system equations do not need to be included in the optimization problem, since they are evaluated implicitly by the physical system [10, 12]. Previous works on FO have proved the convergence of the iterative solution method to the set of local optima under certain conditions [10–12] and provide stability [13] and robustness [14] certificates for FO.

This work focuses on emergency power system operation. Emergency operation is characterized by events happening on fast timescales which lead to transients in the power system (e.g., cascading outages) [5]. To control the power system in this mode, a controller needs to act fast enough and needs to be robust against model inaccuracies, because cascading outages can cause the power system in emergency mode to change rapidly. Therefore, in this work, FO is operated beyond current stability constraints by firstly pushing the principle of FO acting on a different timescale from the remaining dynamics of the power system to the limit and secondly operating FO with inaccurate model information. Because of the timescales and the transients of emergency operation, the simulations in this project take into account power system dynamics.

The remainder of this thesis is structured as follows: In chapter 2 the used static and dynamic power system models are presented, before chapter 3 describes the implemented FO controller and an approach to guarantee convergence thereof. Chapter 4 presents and discusses the simulation set-up and the obtained simulation results. Finally, the thesis is concluded in chapter 5.

Chapter 2

Power System Modelling

This chapter describes the power system models used in this project. Section 2.1 presents the admittance matrix used to model the network of the power system. The static power flow solution is reviewed in section 2.2, before introducing the dynamic power system model in the subsequent section 2.3. To simulate power systems and their dynamics, multiple simulation environments were tested. They are reviewed shortly in section 2.4. After testing different simulation environments, the software package *DynPSSimPy* is used during this project.

2.1 Power System Admittance Matrix

The nodal admittance matrix of a power system contains the information of the topology of the power system (i.e., the admittances between the nodes). During this report, two types of admittance matrices are used: the admittance matrix for the dynamic system \mathbf{Y} and the admittance matrix for the static system \mathbf{Y}_{PF} . They are both complex valued square matrices $\mathbf{Y}, \mathbf{Y}_{PF} \in \mathbb{C}^{b \times b}$, where b is the number of buses in the power system. However, some entries of \mathbf{Y} and \mathbf{Y}_{PF} differ slightly, which will be explained in the following. For the sake of simplicity, transmission lines and transformers are referred to as branches in this report.

The off-diagonal elements of the static admittance matrix \mathbf{Y}_{PF} are given by

$$Y_{PF,ij} = -\bar{t}_{ij}t_{ji}y_{ij}. \quad (2.1)$$

Thereby $y_{ij} = 1/(r_{ij} + jx_{ij}) \in \mathbb{C}$ is the admittance between bus i and j given by the transmission line or transformer resistance r_{ij} and reactance x_{ij} , that connect the two buses, and $t_{ij} = a_{ij}e^{j\phi_{ij}}$ is the voltage ration of the connection between the two buses. For a transmission line $t_{ij} = 1$, while for a transformer $a_{ij} \in \mathbb{R}$ and $\phi_{ij} \in \mathbb{R}$ are the voltage magnitude ratio and the induced phase shift, respectively. The diagonal entries of the static admittance matrix \mathbf{Y}_{PF} are computed as follows

$$Y_{PF,ii} = y_i^{sh} + \sum_{j \in \Omega_i} a_{ij}^2 \left(\frac{y_{ij}^{sh}}{2} + y_{ij} \right), \quad (2.2)$$

where y_i^{sh} and y_{ij}^{sh} are the complex valued shunt admittances at the bus i and of the branch connecting bus i to bus j , and Ω_i is the set of buses adjacent to bus i .

The admittance matrix of the dynamic system \mathbf{Y} is based on the admittance matrix of the static system \mathbf{Y}_{PF} . The difference is that additional terms, corresponding to the generators and the loads in the network, are added to the diagonal entries of the dynamic system admittance matrix \mathbf{Y} .

When comparing the power flow equations of the dynamic simulation, that will be presented in equation (2.20), with the power flow equations of the static power flow, which will be introduced

in equations (2.7) and (2.14), one can observe, that the loads are included only on the right-hand side of the static power flow equations. The dynamic power flow equations are based on the currents, which makes it easier to incorporate the generators as equivalent current sources. As a consequence, loads are modelled as impedances in the dynamic system. Therefore their admittance $y_{i,l}$ is added to the diagonal elements of the dynamic admittance matrix \mathbf{Y} as shown in equation (2.4). The load admittance $y_{i,l}$ is determined from the known active and reactive power injections at the loads $p_{set,i}$ and $q_{set,i}$, respectively, and the bus voltage u_i

$$y_{i,l} = \frac{-\bar{s}_i}{||u_i||^2} = \frac{-p_{set,i} + jq_{set,i}}{||u_i||^2}. \quad (2.3)$$

The simulated power systems are assumed to comprise multiple generators. Since each generator under interest has a much smaller power rating compared to the other generators in the system, the remaining power system is modelled as an infinite bus, connected to the generator by an equivalent system [7]. The equivalent system thereby is represented by the transmission system and the remaining generators in the power system. Therefore, the Norton equivalent reactance of the generators $y_{i,g} = \frac{1}{jX_d''}$, where X_d'' is given by the synchronous machine (see section 2.3.1), is added to the static admittance matrix \mathbf{Y}_{PF} to obtain the dynamic admittance matrix \mathbf{Y} as shown in equation (2.4).

$$Y_{ii} = Y_{PF,ii} + y_{i,l} + y_{i,g} \quad (2.4)$$

2.2 Static Power Flow Solution

The static power flow equations will be used for two reasons during this thesis. To initialize the states of the dynamic power system models, and to derive the sensitivities for the FO controller. This section presents the classical power flow solution, before an extension to it to model a distributed slack is introduced in section 2.2.1. These final power flow equations are used during this project.

Static power flow solutions are based on the following set of complex valued power flow equations [7]

$$\text{diag}(\mathbf{u})\overline{\mathbf{Y}_{PF}\mathbf{u}} - \mathbf{s} = 0, \quad (2.5)$$

where $\mathbf{s} \in \mathbb{C}^b$ is a vector of the complex power injections at each bus, given by the generation and load at that bus. The static system admittance matrix \mathbf{Y}_{PF} is given by the network topology, as described in the previous section. By splitting up the complex voltages \mathbf{u} and power injections \mathbf{s} into voltage magnitudes \mathbf{v} and angles $\boldsymbol{\theta}$ and active and reactive power injections \mathbf{p} and \mathbf{q} , respectively, using the following identities

$$\mathbf{u} = \mathbf{v}e^{j\boldsymbol{\theta}} \quad (2.6a)$$

$$\mathbf{s} = \mathbf{p} + j\mathbf{q}, \quad (2.6b)$$

the power flow equations (2.5) can be separated in their real and imaginary part as follows

$$\mathbf{F}'(\mathbf{u}, \mathbf{p}, \mathbf{q}) = \begin{bmatrix} \Re(\text{diag}(\mathbf{u})\overline{\mathbf{Y}_{PF}\mathbf{u}}) - \mathbf{p} \\ \Im(\text{diag}(\mathbf{u})\overline{\mathbf{Y}_{PF}\mathbf{u}}) - \mathbf{q} \end{bmatrix} = 0. \quad (2.7)$$

As can be seen in equations (2.6), the power flow problem has a total number of $4b$ variables (v , θ , p , and q for each bus), while equation (2.7) provides $2b$ equations. Therefore, for each bus two more equations are needed and given by already known properties dependent on the type of bus:

PV bus Generators are assumed to control their bus voltage magnitude to a preset value $v_{set,i}$ and produce the scheduled amount of active power $p_{set,i}$. Therefore, each bus i connected to a generator has fixed bus voltage magnitude v_i and active power injection p_i

$$v_i = v_{set,i} \quad (2.8a)$$

$$p_i = p_{set,i}. \quad (2.8b)$$

The voltage angle θ_i and reactive power injection q_i remain as free variables.

PQ bus Each bus i without a generator is assumed to have active and reactive power injections $p_{set,i}$ and $q_{set,i}$, respectively, independent of the system variables. Therefore the active and reactive power injections at this bus p_i and q_i , respectively, are fixed as follows

$$p_i = p_{set,i} \quad (2.9a)$$

$$q_i = q_{set,i}. \quad (2.9b)$$

The power injections can be derived from the power withdrawals of the loads connected to the bus or set to zero if no power is injected or withdrawn at this bus. The voltage magnitude v_i and voltage angle θ_i remain as free variables.

Slack bus Since the active power losses in the power system are a function of the network voltages \mathbf{u} , a possible imbalance resulting from losses and imbalanced active power injections of the power system is unknown a priori. Therefore, one generator-bus in the system needs to be defined to compensate for the system imbalance ψ and needs p_i as a free variable. The voltage magnitude of the bus v_i still is controlled to a preset value $v_{set,i}$ by the generator. Furthermore, a reference point for the voltage angles $\boldsymbol{\theta}$ is necessary to obtain a unique solution to the power flow equations. This reference point is set to be the same bus, that compensates the system losses. Defining a different bus as angle reference would shift the voltage angles in the power system, but not change the load flow. Hence, the following additional equations for the slack bus yield:

$$v_i = v_{set,i} \quad (2.10a)$$

$$\theta_i = 0. \quad (2.10b)$$

With that, the active and reactive power injections p_i and q_i , respectively, remain free variables.

For completeness and later use, the free variables are referred to as power flow output variables \mathbf{z}_{PF} , and the fixed variables as power flow input variables \mathbf{w}_{PF} . With the above described equations additional to the power flow equations (2.7), all variables $\mathbf{v}, \boldsymbol{\theta}, \mathbf{p}$ and \mathbf{q} of the static power system can be determined. Based on these variables, all properties of the static power system can be computed. The current on a branch i_{ij} connecting two buses i and j , for instance, is given by

$$i_{ij} = a_{ij}^2 \left(\frac{y_{ij}^{sh}}{2} + y_{ij} \right) u_i - a_{ij} \bar{a}_{ji} y_{ij} u_j. \quad (2.11)$$

2.2.1 Modelling of Distributed Slack

As mentioned above, the active power losses in the power system p_{loss} are unknown as long as the state of the power system is not determined. Furthermore, there could be an imbalance in active power injections

$$\Delta p = \sum_{i \in [1,b]} p_i, \quad (2.12)$$

which adds to the total system imbalance $\psi \in \mathbb{R}$ as follows

$$\psi = p_{loss} - \Delta p. \quad (2.13)$$

Since the power system is assumed to be in steady state in the static power flow solution, the imbalance ψ needs to be compensated.

In practice, an AGC as described in section 2.3.2 acts on the system to balance the active power generation. The AGC estimates the imbalance ψ and distributes it according to the AGC participation factors α to the generators. Thereby the system imbalance ψ is compensated by multiple generators at different buses.

This contrasts the above described classical approach of solving the power flow equations. Therefore, the power flow equations are extended by a distributed slack approach as described in [15], which leads to the following new power flow equations

$$\mathbf{F}(\mathbf{u}, \mathbf{p}, \mathbf{q}, \psi) = \begin{bmatrix} \Re(\text{diag}(\mathbf{u})\overline{\mathbf{Y}_{PF}\mathbf{u}}) - \mathbf{p} - \boldsymbol{\pi}\psi \\ \Im(\text{diag}(\mathbf{u})\overline{\mathbf{Y}_{PF}\mathbf{u}}) - \mathbf{q} \end{bmatrix} = 0, \quad (2.14)$$

where $\boldsymbol{\pi} \in \mathbb{R}^b$ is a vector of the sum of the AGC participation factors per generator, α , per bus, i.e.,

$$\pi_i = \sum_{\text{Generator } j \text{ at bus } i} \alpha_j. \quad (2.15)$$

As the AGC participation factors per generator α_i sum up to 1 (see section 2.3.2), the sum of the participation factors per bus π_i will sum to 1 as well $\sum_{i \in [1, b]} \pi_i = 1$.

Since an additional variable ψ modelling the total system imbalance is added to the system of equations, we require an additional equation compared to the above classical approach. By distributing the imbalance ψ over multiple generators, there is no single slack bus as in the classical approach anymore. Instead, an angle reference bus is introduced. The former slack bus is treated as a PV bus with fixed active power injection, which yields the required additional equation:

PV bus All generator buses have fixed bus voltage magnitude v_i and scheduled active power injection p_i as described in equations (2.8). See remark 1 regarding the meaning of the variable p_i in the distributed slack case.

PQ bus All the remaining buses are assumed to have fixed active and reactive power injections p_i and q_i , respectively, as shown in equations (2.9).

Angle reference bus In order to obtain a unique solution to the power flow equations, a reference point for the voltage angles $\boldsymbol{\theta}$ is still necessary. This leads to the following additional equation for the angle reference bus i

$$\theta_i = 0. \quad (2.16)$$

Note, that the power flow equations for the distributed slack are equivalent to the classical power flow equations for $\boldsymbol{\pi}$ being a one-hot vector as follows

$$\pi_i = \begin{cases} 1 & \text{if } i \text{ is the slack bus} \\ 0 & \text{otherwise} \end{cases}. \quad (2.17)$$

Remark 1. Since in the distributed slack version of the power flow equations, the right-hand side of the active power balance in equation (2.7), is replaced by $\mathbf{p} + \boldsymbol{\pi}\psi$ in equation (2.14),

the variables \mathbf{p} do not represent the active power injections per bus anymore, as in the classical approach. The active power injections in the case of the distributed slack \mathbf{p}_{dist} are given by

$$\mathbf{p}_{dist} = \mathbf{p} + \boldsymbol{\pi}\psi. \quad (2.18)$$

The variable \mathbf{p} can be interpreted as scheduled active power injections in this case, while the term $\boldsymbol{\pi}\psi$ represents the unscheduled active power injections.

2.3 Dynamic Power System Model

This section presents the dynamic power system simulation with the used power flow equations and models of the components. The equations are based mostly on [7, 16, 17] and completed by inquires with the authors of [16].

The model of the dynamic power system can be written as a system of differential algebraic equations (DAE) depending on the states $\mathbf{x} \in \mathbb{R}^n$ of the dynamic power system model, the complex bus voltages $\mathbf{u} \in \mathbb{C}^b$ and some parameters \mathbf{w}

$$\dot{\mathbf{x}} = \mathbf{f}'(\mathbf{x}, \mathbf{u}, \mathbf{w}) \quad (2.19a)$$

$$0 = \boldsymbol{\sigma}(\mathbf{x}, \mathbf{u}), \quad (2.19b)$$

where \mathbf{f}' and $\boldsymbol{\sigma}$ represent the state evolution and network equation of the power system and n and b are the number of states and buses in the dynamic power system, respectively. Note, that the bus voltages \mathbf{u} are no state variables of the dynamic power system, because they result from the states of the dynamic power system model through the current injections, as will be introduced below. The parameters \mathbf{w} represent the control inputs and will be described in section 3.2.

The algebraic network equation $\boldsymbol{\sigma}$ can be expressed as follows

$$\boldsymbol{\sigma}(\mathbf{x}, \mathbf{u}) = \mathbf{Y}\mathbf{u} - \mathbf{i}_{inj}(\mathbf{x}), \quad (2.20)$$

using the dynamic system admittance matrix \mathbf{Y} and a function $\mathbf{i}_{inj}(\mathbf{x})$ representing the currents injected at each bus by the generators dependent on the system state \mathbf{x} . Since $\boldsymbol{\sigma}(\mathbf{x}, \mathbf{u})$ is linear in \mathbf{u} , the bus voltages \mathbf{u} can be eliminated in the system of DAE (2.19). This leads to the following system of ordinary differential equations (ODE)

$$\dot{\mathbf{x}} = \mathbf{f}'(\mathbf{x}, \mathbf{u}(\mathbf{x}), \mathbf{w}) = \mathbf{f}(\mathbf{x}, \mathbf{w}), \quad (2.21)$$

with $\mathbf{u}(\mathbf{x}) = \mathbf{Y}^{-1}\mathbf{i}_{inj}(\mathbf{x})$. The function $\mathbf{f}'(\mathbf{x}, \mathbf{u}, \mathbf{w})$, which describes the state evolution, and the current injections $\mathbf{i}_{inj}(\mathbf{x})$ depend on the used models for the simulated power system components and will be described in the following paragraphs.

The state evolution $\mathbf{x}(t)$ is obtained by integrating the ODE system (2.21) starting from an initial state $\mathbf{x}_0 \in \mathbb{R}^n$. The initial state \mathbf{x}_0 of the power system is chosen such that the system is in equilibrium and determined by solving the following algebraic equation for \mathbf{x}_0

$$0 = \mathbf{f}'(\mathbf{x}_0, \mathbf{u}_0, \mathbf{w}_0), \quad (2.22)$$

where \mathbf{u}_0 are the initial system voltages determined by running a static power flow computation on the power system, as described in the previous section, and \mathbf{w}_0 is the initial control input.

2.3.1 Synchronous Machine

This section presents the dynamic models of the synchronous machine and its governor, excitation system and power system stabilizer (PSS). A sixth-order-model of the synchronous machine [7,

[16] is used in this project. The states are given by the speed deviation of the rotor speed from the nominal frequency $\Delta\omega$, the rotor angle δ and the internal voltages E'_q , E'_d , E''_q and E''_d . The state space representation of the synchronous machine is shown in equations (2.23). Equation (2.23a) is extended compared to the model given in [7] by adding the influence of the damping of the synchronous machine via the damping coefficient D [18] and not neglecting the difference between the speed of synchronous machine ω and the synchronous speed (which equals 1 p.u.). This leads to an implemented synchronous machine model consistent with professional dynamic power system simulators such as *PowerFactory* by *DIgSILENT* [19].

$$\Delta\dot{\omega} = \frac{1}{2H} \left(\frac{p_m}{\omega} - p_e - D\omega \right) \quad (2.23a)$$

$$\dot{\delta} = \Delta\omega \quad (2.23b)$$

$$\dot{E}'_q = \frac{E_f - E'_q - I_d(X_d - X'_d)}{T'_{d0}} \quad (2.23c)$$

$$\dot{E}'_d = \frac{-E'_d + I_q(X_q - X'_q)}{T'_{q0}} \quad (2.23d)$$

$$\dot{E}''_q = \frac{E'_q - E''_q - I_d(X'_d - X''_d)}{T''_{d0}} \quad (2.23e)$$

$$\dot{E}''_d = \frac{E'_d - E''_d + I_q(X'_q - X''_q)}{T''_{q0}} \quad (2.23f)$$

$$(2.23g)$$

The variables H , D , X_d , X'_d , X''_d , X_q , X'_q , X''_q , T'_{d0} , T'_{q0} , T''_{d0} , and T''_{q0} are positive, real valued parameters of the synchronous machine and described in table 2.1. The mechanical power p_m and field voltage E_f are given by the outputs of the governor and excitation system models corresponding to this synchronous machine, respectively (see following paragraphs). The electrical power output p_e of the synchronous machine is given by

$$p_e = E''_d I_d + E''_q I_q, \quad (2.24)$$

where $X''_d \approx X'_d$ is assumed, i.e., *subtransient saliency* is neglected, which is reasonable for a synchronous machine having a damper winding in the direct-axis and quadrature-axis direction¹ [7]. The direct-axis and quadrature-axis currents I_d and I_q , respectively, used in equations (2.23) and (2.24) are given by the following equation [7, 16]

$$\begin{bmatrix} R & X''_d \\ -X''_d & R \end{bmatrix} \begin{bmatrix} I_d \\ I_q \end{bmatrix} = \begin{bmatrix} E''_d \\ E''_q \end{bmatrix} - \begin{bmatrix} v_d \\ v_q \end{bmatrix}, \quad (2.25)$$

where R is the armature winding resistance and v_d and v_q are the real and imaginary part of the bus voltage, respectively [16]

$$v_d = \text{Re}(u_i) \quad (2.26a)$$

$$v_q = \text{Im}(u_i). \quad (2.26b)$$

In the interconnection of the synchronous machine with the transmission network, the synchronous machine is modelled with its Norton equivalent circuit [16]. The injected current is given by

$$i_{inj} = - \left(\frac{E''_d}{X''_d} + j \frac{E''_q}{X''_q} \right) e^{j\delta}. \quad (2.27)$$

¹The direct- and quadrature-axis are the two axis of the rotor of a synchronous machine. The direct axis points into the direction of the magnetic field of the field windings. The quadrature-axis is shifted by $\pi/2$ radians behind the direct-axis. [7]

Parameter	Description
H	Inertia constant
D	Damping coefficient
X_d	Direct-axis synchronous reactance
X'_d	Direct-axis transient reactance
X''_d	Direct-axis subtransient reactance
X_q	Quadrature-axis synchronous reactance
X'_q	Quadrature-axis transient reactance
X''_q	Quadrature-axis subtransient reactance
R	Armature winding resistance
T'_{d0}	Direct-axis transient open-circuit time constant
T'_{q0}	Quadrature-axis transient open-circuit time constant
T''_{d0}	Direct-axis subtransient open-circuit time constant
T''_{q0}	Quadrature-axis subtransient open-circuit time constant

Table 2.1: Parameters of the synchronous machine model [7].

Governor

The governor used to control the mechanical power p_m fed to the synchronous machine is modelled with the standard model *TGOV1* [16, 20]. The state-space representation of the governor is given in equations (2.28). x_1 and x_2 are states of the governor representing the valve position and the turbine power, respectively. Due to saturation effects, the state x_1 is constraint to stay in the range $[V_{min}, V_{max}]$. Furthermore, $x_{bias} = Rp_{m0}$, with p_{m0} being the steady state active power fed into the network by the corresponding synchronous machine, is added to the frequency deviation $\Delta\omega$ in order to eliminate a steady state error of the proportional controller at the initial state of the power system. $T_1, T_2, T_3, R, D_t, V_{min}$ and V_{max} are parameters of the governor and described in table 2.2.

$$\dot{x}_1 = \begin{cases} 0 & \text{for } x_1 = V_{min} \wedge \dot{x}_1 < 0 \text{ or } x_1 = V_{max} \wedge \dot{x}_1 > 0 \\ \frac{1}{T_1 R}(\Delta\omega + x_{bias}) - \frac{x_1}{T_1} & \text{otherwise} \end{cases} \quad (2.28a)$$

$$\dot{x}_2 = \left(\frac{T_2}{T_3} - 1\right)x_1 - \frac{1}{T_3}x_2 \quad (2.28b)$$

The mechanical power output p_{GOV} of the governor model is given by

$$p_{GOV} = \frac{T_2}{T_3}x_1 - \frac{1}{T_3}x_2 - D_t\Delta\omega. \quad (2.29)$$

It is used, besides other components, as part of the mechanical power input p_m of the synchronous generator in equation (2.23a). The governor model's input-output relation is displayed as block diagram in figure 2.1.

Parameter	Description
T_1	Governor time constant
T_2, T_3	Turbine time constants
R	Turbine governor droop
D_t	Frictional losses factor
V_{min}, V_{max}	Valve limits

Table 2.2: Parameters of the governor model [20].

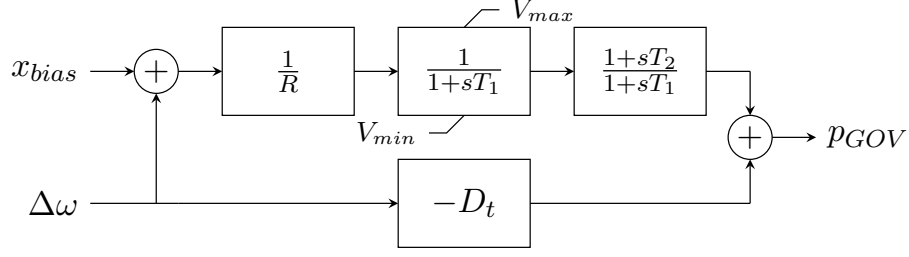


Figure 2.1: Block diagram of governor model *TGOV1*.

Excitation System

The field voltage E_f of the synchronous machine is controlled by the excitation system. Therefore the standard model *SEXS* (simple excitation system) is applied [16, 20]. To enhance small- and large-signal stability of the excitation system, a power system stabilizer of the type *STAB1* controls the input of the excitation system [7, 16].

The excitation system has the two states x_1 and e_f , where e_f is the unsaturated field voltage. The state evolution is given in its state space representation in equations (2.30) and the parameters of the excitation system are described in table 2.3.

$$\dot{x}_1 = -\frac{1}{T_b}x_1 + \left(\frac{T_a}{T_b} - 1\right)u \quad (2.30a)$$

$$\dot{e}_f = -\frac{K}{T_e T_b}x_1 - \frac{1}{T_e}e_f + \frac{KT_a}{T_e T_b}u \quad (2.30b)$$

The output of the excitation system is the field voltage E_f after saturation of the internal voltage e_f as follows

$$E_f = \begin{cases} E_{max} & \text{for } e_f > E_{max} \\ e_f & \text{for } e_f \in [E_{min}, E_{max}] \\ E_{min} & \text{for } e_f < E_{min} \end{cases}, \quad (2.31)$$

where E_{min} and E_{max} are the lower and upper field voltage limits, respectively.

The input u to the excitation system model shown in equations (2.30) is given by adding the deviation of the bus voltage magnitude v from the voltage set point v_{set} , the output of the PSS v_{pss} and a constant bias x_{bias}

$$u = \Delta v + v_{pss} + x_{bias} = v_{set} - v + v_{pss} + x_{bias}. \quad (2.32)$$

Similar as in the governor model, the constant bias $x_{bias} = \frac{E_{f0}}{K}$ is added to ensure error-free tracking at the initial state. The block diagram of the excitation system model is pictured in figure 2.2.

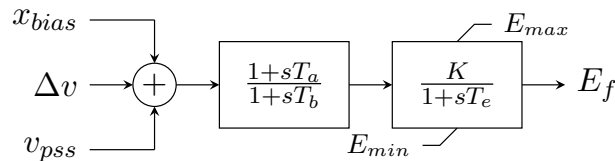


Figure 2.2: Block diagram of the excitation system model *SEXS*.

Parameter	Description
K	Controller gain
T_a, T_b	Filter time constants
T_e	Exciter time constant
E_{min}, E_{max}	Field voltage limits

Table 2.3: Parameters of the excitation system model [20].

The excitation system is stabilized by adding the extra term v_{pss} from the PSS to the excitation system input. The PSS model *STAB1* is considered in this project. It takes the generator's speed deviation $\Delta\omega$ as input and returns v_{pss} as output. The state space representation is displayed in equations (2.33).

$$\dot{x}_1 = -\frac{1}{T}x_1 + \frac{1}{T}\Delta\omega \quad (2.33a)$$

$$\dot{x}_2 = -\left(\frac{T_1}{T_3} - 1\right)x_1 - \frac{1}{T_3}x_2 + \left(\frac{T_1}{T_3} - 1\right)\frac{K}{T}\Delta\omega \quad (2.33b)$$

$$\dot{x}_3 = -\left(\frac{T_2}{T_4} - 1\right)\frac{T_1}{T_3}\frac{1}{T}x_1 - \left(\frac{T_2}{T_4} - 1\right)\frac{1}{T_3}x_2 - \frac{1}{T_4}x_3 + \left(\frac{T_2}{T_4} - 1\right)\frac{T_1}{T_3}\frac{1}{T}\Delta\omega \quad (2.33c)$$

The states x_1 , x_2 and x_3 are not connected a physical quantity, but represent the state of the PSS after the washout-filter (x_1) and after the two lead-lag compensators (x_1 and x_2 , respectively). v_{pss} , which is the output of the PSS, is computed based on those states as follows:

$$v_{pss} = \begin{cases} H_{lim} & \text{for } y > H_{lim} \\ y & \text{for } y \in [-H_{lim}, H_{lim}] \\ -H_{lim} & \text{for } y < -H_{lim} \end{cases}, \quad (2.34a)$$

$$y = -\frac{T_2}{T_4}\frac{T_1}{T_3}\frac{1}{T}x_1 - \frac{T_2}{T_4}\frac{T_1}{T_3}x_2 - \frac{1}{T_4}x_3 + \frac{T_2}{T_4}\frac{T_1}{T_3}\frac{K}{T}\Delta\omega. \quad (2.34b)$$

The parameters of the PSS are described in table 2.4 and the block diagram of the PSS is shown in figure 2.3.

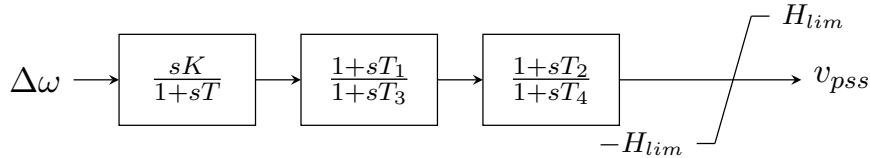


Figure 2.3: Block diagram of the power system stabilizer *STAB1*.

Parameter	Description
K	Controller gain
T	Washout-filter time constant
T_1, T_3	Time constants of first lead-lag compensation
T_2, T_4	Time constants of second lead-lag compensation
H_{lim}	Output limit

Table 2.4: Parameters of the power system stabilizer model.

2.3.2 Automated Generation Control

To balance the active power generation and consumption in the power system, an automated generation control (AGC) is needed. The used AGC is acting only on frequency deviations and ignores unscheduled tie line flows. Therefore, the area control error ACE is computed as follows

$$ACE = -\lambda\Delta\bar{\omega}, \quad (2.35)$$

where λ is the frequency bias factor and $\Delta\bar{\omega}$ is the average frequency deviation over all g generators in the simulated power system weighted by their inertia constant H and power rating S

$$\Delta\bar{\omega} = \frac{\sum_{i \in [1,g]} \Delta\omega_i H_i S_i}{\sum_{i \in [1,g]} H_i S_i}. \quad (2.36)$$

The AGC integrates the area control error ACE in the state x_i and returns the vector $\mathbf{p}_{AGC} \in \mathbb{R}^g$ according to equations (2.37). The i th entry in \mathbf{p}_{AGC} represents the control signal for generator i in the power system and is added to the mechanical power input p_m of the corresponding synchronous generator in equation (2.23a).

$$\dot{x}_i = ACE \quad (2.37a)$$

$$\mathbf{p}_{AGC} = \boldsymbol{\alpha}(K_p ACE + K_i x_i) \quad (2.37b)$$

The parameters λ , K_p , and K_i are described in table 2.5 and figure 2.4 displays the block diagram of the AGC. The vector $\boldsymbol{\alpha} \in \mathbb{R}^g$ contains the participation factor of each generator and is used to distribute the control signal of the AGC to the participating generators. The sum of all entries α_i of $\boldsymbol{\alpha}$ equals one: $\sum_{i \in [1,g]} \alpha_i = 1$. A deviation of this sum from 1 would be compensated by the integral part of the AGC, however, it would slow down convergences of the frequency.

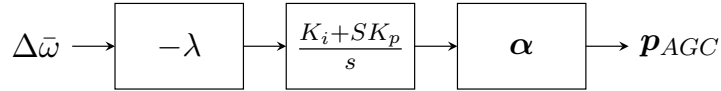


Figure 2.4: Block diagram of the automated generation control.

Parameter	Description
λ	Frequency bias factor
K_p	Proportional gain
K_i	Integral gain

Table 2.5: Parameters of the automated generation control model [7].

2.4 Review on Dynamic Power System Simulators

Only few open source or free to use dynamic power system simulators are available. Among those, the following toolboxes, which have an interface to or are written entirely in Python are reviewed in the following: *RAMSES* [21] with its python interface *PyRAMSES* [22], *DP-Sim* [23], and *DynPSSimPy* [16, 17]. Table 2.6 presents the version, the programming language and references for the considered simulators. The power system simulator *RAMSES* has been developed at the University of Liège, Belgium, and *DPSim*, at the RWTH Aachen University, Germany. The implementations of *PyRAMSES* and *DPSim* in FORTRAN and C++, respectively, allow for fast and efficient computations. This contrasts the third dynamic power system simulator, *DynPSSimPy*, which has been developed at the Norwegian university of science and

technology and is entirely written in Python. All three simulation environments come with the downside of poor documentation. While the simulators *PyRAMSES* and *DPSim* with their efficient implementation in different programming languages are hard to retrace, the less efficient implementation of *DynPSSimPy* in Python is fully transparent, easily tractable, and extendable. This compensates the lack in documentation and is the main reason for using *DynPSSimPy* in this project.

Simulator	Version	Programming language	Reference
<i>PyRAMSES</i>	0.0.22	FORTRAN, Python interface	[21, 22] pyramses.paristidou.info
<i>DPSim</i>	1.0.0	C++, Python interface	[23] dpsim.fein-aachen.org
<i>DynPSSimPy</i>	0.1.0	Python	[16, 17] github.com/hallvar-h/DynPSSimPy

Table 2.6: Comparison of dynamic power system simulators.

The simulation environment *DynPSSimPy* provides the models of the power system components described in the last section. It is modulated in three aspects for the use in this project. In order to be consistent with the dynamic simulations, the existing power flow solver in *DynPSSimPy* is extended by the distributed slack approach described in section 2.2.1. Out of the box, *DynPSSimPy* models loads with constant impedances, i.e., it determines the load admittances once with the initial voltages \mathbf{u}_0 and does not update them. In order to be consistent to the static power flow simulation, the admittances are updated every iteration to model the loads with constant power. Lastly, the AGC provided in *DynPSSimPy* is capable of balancing only two control areas connected by one transmission line. It is modified slightly in order to support multiple control areas but act only on frequency deviations.

Chapter 3

Feedback Optimization for Emergency Operation

To control the dynamic power system modelled as described in chapter 2 in emergency operation, a feedback optimization (FO) controller is applied. This chapter therefore reviews FO in section 3.1 and applies it to the problem of controlling a power system in section 3.2. In section 3.3, the tuning of the FO controller is discussed.

3.1 Review of Feedback Optimization

Consider a stable physical system

$$\dot{\mathbf{x}} = \mathbf{f}(\mathbf{x}, \mathbf{w}) \quad (3.1a)$$

$$\mathbf{z} = \mathbf{g}(\mathbf{x}), \quad (3.1b)$$

where $\mathbf{x} \in \mathbb{R}^n$, $\mathbf{w} \in \mathbb{R}^l$ and $\mathbf{z} \in \mathbb{R}^m$ are the states, inputs and outputs of the physical system, respectively. The behavior of the system is described by the function $\mathbf{f} : \mathbb{R}^{n \times l} \rightarrow \mathbb{R}^n$ and the output is given by the map $\mathbf{g} : \mathbb{R}^n \rightarrow \mathbb{R}^m$. The goal is to drive the system (3.1) to an operating point $(\mathbf{w}^*, \mathbf{z}^*)$ that solves the optimization problem (3.2). Namely, $(\mathbf{w}^*, \mathbf{z}^*)$ minimize the continuously differentiable objective function $\Phi : \mathbb{R}^{l \times m} \rightarrow \mathbb{R}$, while applying admissible control inputs \mathbf{w} given by the set $\mathcal{W} \subseteq \mathbb{R}^l$ and fulfilling the constraints on the output variables \mathbf{z} given by $\mathcal{Z} \subseteq \mathbb{R}^m$.

$$\min_{\mathbf{w}} \Phi(\mathbf{w}, \mathbf{z}) \quad (3.2a)$$

$$\text{s.t. } \mathbf{z} = \mathbf{h}(\mathbf{w}) \quad (3.2b)$$

$$\mathbf{w} \in \mathcal{W} \quad (3.2c)$$

$$\mathbf{z} \in \mathcal{Z} \quad (3.2d)$$

The map $\mathbf{h} : \mathbb{R}^l \rightarrow \mathbb{R}^m$ in the above equation maps the inputs \mathbf{w} to their steady state outputs \mathbf{z} and results as follows. Since the system (3.1) is assumed to be stable, there exists a $\hat{\mathbf{h}} : \mathbb{R}^l \rightarrow \mathbb{R}^n$ that maps an input \mathbf{w} to the corresponding steady state value of the state vector \mathbf{x} such that

$$\mathbf{f}(\hat{\mathbf{h}}(\mathbf{w}), \mathbf{w}) = 0. \quad (3.3)$$

The steady state map \mathbf{h} is then defined as

$$\mathbf{h}(\mathbf{w}) = \mathbf{g}(\hat{\mathbf{h}}(\mathbf{w})). \quad (3.4)$$

Traditional approaches to solve the above optimization problem (3.2) use a model for $\mathbf{h}(\mathbf{w})$, solve for the optimal control input \mathbf{w}^* , and apply it to the physical system in order to drive it to the optimal operating point $(\mathbf{w}^*, \mathbf{z}^*)$. This feed-forward approach is computationally expensive and requires an accurate model of the steady state map \mathbf{h} . A controller using this approach is implemented as a benchmark in section 4.1.2. In contrast to that, FO approaches exploit the ability of the physical system to enforce constraint (3.2b) of the optimization problem by its own and use measurements of the output variables \mathbf{z} to drive the system iteratively to the optimal operating point $(\mathbf{w}^*, \mathbf{z}^*)$. Thereby the FO solution methods are computationally less expensive and model-free, since $\mathbf{z} = \mathbf{h}(\mathbf{w})$ is evaluated by the physical system. However, some information on the physical system (3.1) is needed, as will be described in the following section.

3.1.1 Projected Gradient Descent Flow

In this thesis, the discrete time integral feedback control law proposed in [24] is used to solve the optimization problem (3.2). The control input at iteration $k + 1$ of the controller is given by

$$\mathbf{w}_{k+1} = \mathbf{w}_k + \alpha \Delta \mathbf{w}_\alpha^*(\mathbf{w}_k, \mathbf{z}) \quad (3.5)$$

for $k \in \mathbb{N}_0$, where $\alpha > 0$ is a positive step size, and $\Delta \mathbf{w}^* \in \mathbb{R}^l$ is the minimizing argument of the following quadratic program (QP)

$$\Delta \mathbf{w}_\alpha^*(\mathbf{w}, \mathbf{z}) = \arg \min_{\Delta \mathbf{w} \in \mathbb{R}^l} \left\| \Delta \mathbf{w} + \mathbf{G}^{-1}(\mathbf{w}) \mathbf{H}(\mathbf{w})^T \nabla \Phi(\mathbf{w}, \mathbf{z})^T \right\|_{\mathbf{G}(\mathbf{w})}^2 \quad (3.6a)$$

$$\text{s.t.} \quad \mathbf{w} + \alpha \Delta \mathbf{w} \in \mathcal{W} \quad (3.6b)$$

$$\mathbf{z} + \alpha \nabla \mathbf{h}(\mathbf{w}) \Delta \mathbf{w} \in \mathcal{Z}, \quad (3.6c)$$

where $\mathbf{G}(\mathbf{w})$ is a continuous metric, and $\mathbf{H}(\mathbf{w})^T = [\mathbb{I}_l \quad \nabla \mathbf{h}(\mathbf{w})^T]$ with the Jacobian matrix $\nabla \mathbf{h}$ of the steady state map \mathbf{h} . The metric \mathbf{G} can be a fixed matrix in the set of symmetric positive definite of shape $l \times l$, \mathbb{S}_+^l , or be dependent on the input \mathbf{w} by mapping to this set $\mathbf{G} : \mathcal{W} \rightarrow \mathbb{S}_+^l$. It does not change the optimal points of (3.2), but the trajectory in which these points are reached [12]. The norm $\|\mathbf{b}\|_{\mathbf{G}(\mathbf{w})}$ for some $\mathbf{b} \in \mathbb{R}^l$ evaluates as

$$\|\mathbf{b}\|_{\mathbf{G}(\mathbf{w})} = \sqrt{\mathbf{b}^T \mathbf{G}(\mathbf{w}) \mathbf{b}}. \quad (3.7)$$

The system output \mathbf{z} is given by measurements of the physical system, and thus no exact model of the steady state map \mathbf{h} is needed. To solve the QP (3.6), it is enough to know the sensitivities of the output variables \mathbf{z} in steady state with respect to a change of the input variables \mathbf{w} given by $\nabla \mathbf{h}$.

The above control law (3.5) is based on the idea of gradient flows, while enforcing the constraints of the optimization problem (3.2) by projecting the points $\mathbf{w} - \alpha \mathbf{G}^{-1}(\mathbf{w}) \nabla \Phi(\mathbf{w}, \mathbf{h}(\mathbf{w}))$ to a linearization of the original constraints of (3.2) around \mathbf{w} (see constraints of (3.6)). It hence represents a *projected gradient flow* [12]. Due to the linearization of the constraints in the QP (3.6), the original constraints can be violated temporarily. However, the constraints are satisfied asymptotically, and the violations can be reduced by reducing the step size α [24]. The asymptotic constraint fulfilment and in general solving of the problem (3.2) using the above control law has been shown in [24] using the following mild assumptions.

Assumption 1. *The feasible set of the optimization problem (3.2) is non-empty and the set of admissible inputs \mathcal{W} is compact.*

This assumption is necessary for the optimization problem (3.2) to have any solution. Furthermore, the set of feasible control inputs \mathcal{W} is assumed to be compact in order to apply the extreme value theorem, which is used to find the optimal point within the constraints [24]. The second assumption targets the control law (3.5).

Assumption 2. *The feasible set of the QP (3.6) is non-empty for all $\mathbf{w} \in \mathcal{W}$ and satisfies the linear independence constraint qualification (LICQ) for all $\Delta\mathbf{w}$ in the feasible set of the QP.*

Again, the feasible set is required to be non-empty for the QP (3.6) to have any solution. Additionally, the LICQ are assumed to be satisfied by all $\Delta\mathbf{w}$ in the feasible set of the QP (3.6) in order for it to be well-defined [24].

With these two assumptions, the control law given in equation (3.5) converges to the first-order optimal points of the optimization problem (3.2):

Theorem 1. *Assume that $\nabla\Phi$ and $\nabla\mathbf{h}$ are globally Lipschitz on \mathcal{W} and that assumptions 1 and 2 hold. There exists a step size limit $\alpha_{max} > 0$ such that for every $\alpha < \alpha_{max}$:*

1. *the trajectory of the control law (3.5) converges to the set of first-order optimal points of the optimization problem (3.2) for any initial input $\mathbf{w}_0 \in \mathcal{W}$ and $\mathbf{z} = \mathbf{h}(\mathbf{w})$,*
2. *an asymptotic stable equilibrium of the control law (3.5) is a strict local minimum of $\Phi(\mathbf{w}, \mathbf{h}(\mathbf{w}))$.*

A proof of the above theorem and a theoretical definition of α_{max} are given in [24]. The step size limit α_{max} is, in general, unknown or hard to compute. Two approaches on estimating it are presented in section 3.3.1 as part of the tuning of the FO controller. Before focusing on that, a FO controller to control power systems is presented in the next section.

Remark 2. Clearly, an optimization problem needs to be feasible in order to find a solution to it using FO or any other solution method. This requirement is captured in assumption 1. Although feasibility and infeasibility are generally linked to optimization and are discussed in relevant literature like [25], a possible method to handle infeasibility is sketched due to its risk to happen during emergency operation, as we will see in section 4.2.2.

The optimization software *Ipopt* [26] used in this project converges in case of infeasibility to a point minimizing the constraint violation [27]. This point allows detecting the constraints causing the infeasibility by their Lagrange multipliers: Since the constraint violation is minimized, the Lagrange multipliers with the highest values correspond to the constraints causing the infeasibility. In case that part of these constraints correspond to engineering constraints, that can be violated temporarily, these constraints can be relaxed and added to the objective function via a penalty function and a high cost $M > 0$. This method is known as *Big-M* method [25]. In the application of controlling a power system with FO, the output constraints summarized in the set \mathcal{Z} can usually be violated temporarily.

Let's consider an example, where the lower limits of the i th and j th output constraints cause the optimization problem (3.2) to be infeasible. The relaxed problem would result to

$$\min_{\mathbf{w}} \Phi(\mathbf{w}, \mathbf{z}) + M \left[(e_{z,min,i} - \mathbf{D}_{z,i}\mathbf{z})^2 + (e_{z,min,j} - \mathbf{D}_{z,j}\mathbf{z})^2 \right] \quad (3.8a)$$

$$\text{s.t.} \quad \mathbf{z} = \mathbf{h}(\mathbf{w}) \quad (3.8b)$$

$$\mathbf{w} \in \mathcal{W} \quad (3.8c)$$

$$\mathbf{z} \in \tilde{\mathcal{Z}}, \quad (3.8d)$$

where $e_{z,min,i}$ is the lower limit of the corresponding i th output constraint, $\mathbf{D}_{z,i}$ is the i th row vector of the constraint matrix \mathbf{D}_z (see following section), and $\tilde{\mathcal{Z}}$ is the relaxed set of output constraints. Although the variable M has to be chosen high enough in order to minimize constraint violations, in the FO set-up choosing a high quadratic cost on an output variable leads to a reduction of the step size limit as we will see in section 3.3.1. This relation needs to be taken into account in order to not destabilize the system by fixing the infeasibility.

3.2 Controlling a Power System with Feedback Optimization

In this section, a FO controller as described above is applied to control a power system. As the notation suggests, the function \mathbf{f} in equation (3.1) is given by the dynamics of the power system described in equation (2.21). The control inputs \mathbf{w} represent the set point of the active power production and the voltage set points of the generators in the power system, $\mathbf{p}_{set} \in \mathbb{R}^g$ and $\mathbf{v}_{set} \in \mathbb{R}^g$, respectively. This yields $\mathbf{w} = [\mathbf{p}_{set}^T \ \mathbf{v}_{set}^T]^T \in \mathbb{R}^{2g}$. With that, the controllable input variables correspond to the same variables as in static power system models. The output is chosen to be the complex bus voltages \mathbf{u} split up in their voltage magnitudes \mathbf{v} and angles $\boldsymbol{\theta}$: $\mathbf{z} = [\mathbf{v}^T \ \boldsymbol{\theta}^T]^T \in \mathbb{R}^{2b}$. Although no voltage angle reference is enforced in the dynamic simulation, these measured bus voltage angles are referenced to the same angle reference bus as in the static power flow equations. Since this shifts all voltage angles by the same amount, the power flow is not changed.

The steady state map \mathbf{h} of the dynamic power system is given by the static power flow equations \mathbf{F} defined in equation (2.14)

$$\mathbf{h}(\mathbf{w}) = \left\{ \mathbf{z} = [\mathbf{v}^T \ \boldsymbol{\theta}^T]^T \in \mathbb{R}^{2b} \mid \mathbf{F}(\mathbf{u}(\mathbf{w}), \mathbf{p}(\mathbf{w}), \mathbf{q}, 0) = 0 \right\}, \quad (3.9)$$

where the steady state system voltages $\mathbf{u}(\mathbf{w})$ are represented by their magnitude \mathbf{v} and angle $\boldsymbol{\theta}$ as in identity (2.6a), and the total system imbalance is set to be $\psi = 0$, since in steady state no imbalance is allowed. Therefore, the sensitivities $\nabla \mathbf{h}$ can be computed using the static power system equations as will be shown in the next section.

The objective function Φ can basically be defined arbitrarily, as long as it satisfies the assumption of being continuously differentiable. In this thesis, quadratic objective functions of the form

$$\Phi(\mathbf{w}, \mathbf{z}) = \mathbf{w}^T \mathbf{Q}_w \mathbf{w} + \mathbf{r}_w^T \mathbf{w} + \mathbf{z}^T \mathbf{Q}_z \mathbf{z} + \mathbf{r}_z^T \mathbf{z} + c \quad (3.10)$$

are considered. The input and output weight matrices and vectors $\mathbf{Q}_w \in \mathbb{R}^{2g \times 2g}$, $\mathbf{Q}_z \in \mathbb{R}^{2n \times 2n}$, $\mathbf{r}_w \in \mathbb{R}^{2g}$, and $\mathbf{r}_z \in \mathbb{R}^{2n}$, respectively, can be defined to minimize the quadratic cost on input or output variables, but also to minimize the difference from one variable to the other or from one variable to a fixed value. The constant term $c \in \mathbb{R}$ in the above equation does not influence the outcome of the optimization problem. It is, however, still included to obtain the cost of the current state by evaluating the objective function.

Finally, the sets \mathcal{W} and \mathcal{Z} in the application of the power system are introduced. The input variables \mathbf{w} are constrained to stay within their operating limits $\mathbf{e}_{w,min}, \mathbf{e}_{w,max} \in \mathbb{R}^{n_w}$

$$\mathcal{W} = \left\{ \mathbf{w} \in \mathbb{R}^{2g} \mid \mathbf{e}_{w,min} \leq \mathbf{D}_w \mathbf{w} \leq \mathbf{e}_{w,max} \right\}, \quad (3.11)$$

where $\mathbf{D}_w \in \mathbb{R}^{n_w \times 2g}$, and n_w is the number of input constraints. Similarly, the output variables \mathbf{z} are restricted to stay within their operating limits $\mathbf{e}_{z,min}, \mathbf{e}_{z,max}$ defined by the matrix $\mathbf{D}_z \in \mathbb{R}^{n_z \times 2b}$. Additionally, operating limits on the absolute value of branch currents $|\mathbf{i}(\mathbf{z})|$, which are a nonlinear function of the output variables (see equation (2.11) for the computation of the branch current), are added to the set of admissible outputs \mathcal{Z} :

$$\mathcal{Z} = \left\{ \mathbf{z} \in \mathbb{R}^{2b} \mid \mathbf{e}_{z,min} \leq \mathbf{D}_z \mathbf{z} \leq \mathbf{e}_{z,max}, \mathbf{i}_{min} \leq |\mathbf{i}(\mathbf{z})| \leq \mathbf{i}_{max} \right\}. \quad (3.12)$$

The QP displayed in equations (3.6) for a general optimization problem is extended by one additional constraint before applying it to the optimization of a power system. Because during the iterations of the FO controller no imbalance of active power generation should be created, the QP is restricted to redispatch active power between the generators

$$\sum_{w_i \text{ corresponding to } p_{set,i}} w_i = 0. \quad (3.13)$$

Since the AGC of the power system would re-balance the system, not adding this additional constraint to the QP would assumably still let the FO controller converge to the optimal solution. However, it would slow down convergence, because the AGC needs to compensate for the created imbalance. Therefore, by restricting the controller to redispatch active power by the constraint (3.13), only the change in system losses needs to be balanced by the AGC and convergence can easily be improved.

The interconnection of the dynamic power system model and the FO controller is depicted in figure 3.1. The block-diagram shows how the FO controller controls the power system via \mathbf{v}_{set} and \mathbf{p}_{FO} . Since there are different controllers acting on the active power generation (governor, AGC and FO controller), \mathbf{p}_{set} computed by the FO controller can not directly be fed to the power system. Instead, an auxiliary input, \mathbf{p}_{FO} , is introduced and controlled such that the mechanical power input to the synchronous machines, \mathbf{p}_m , equals \mathbf{p}_{set} at each iteration of the FO controller

$$\mathbf{p}_{FO} = \mathbf{p}_{set} - \mathbf{p}_{GOV} - \mathbf{p}_{AGC}. \quad (3.14)$$

3.2.1 Computation of Sensitivities

Although the FO approach presented in section 3.1 does not require knowledge of the full power system model, some information on the model, namely the steady state sensitivities $\nabla \mathbf{h} \in \mathbb{R}^{2b \times 2g}$, is needed. The sensitivities represent the change of the output variables \mathbf{z} when changing the input variables \mathbf{w} . With the above input and output variables, the steady state sensitivities are the following

$$\nabla \mathbf{h} = \frac{\partial \mathbf{h}}{\partial \mathbf{w}} = \begin{bmatrix} \frac{\partial \mathbf{v}}{\partial \mathbf{p}_{set}} & \frac{\partial \boldsymbol{\theta}}{\partial \mathbf{p}_{set}} \\ \frac{\partial \mathbf{v}}{\partial \mathbf{v}_{set}} & \frac{\partial \boldsymbol{\theta}}{\partial \mathbf{v}_{set}} \end{bmatrix}. \quad (3.15)$$

While the static power flow equations (2.14) can be solved for the output variables \mathbf{v} and $\boldsymbol{\theta}$, given the input variables \mathbf{p}_{set} and \mathbf{v}_{set} , there is no explicit form of the steady state map \mathbf{h} , that could be differentiated to yield the above derivatives. Since the input variables \mathbf{p}_{set} and \mathbf{v}_{set} equal the variables \mathbf{p} and \mathbf{v} , respectively, of the static power flow equations for buses with a generator, all the variables in the above definition of the sensitivities are variables of the static power flow equations \mathbf{F} (2.14). Therefore, the explicit function theorem can be applied to the static power flow equations \mathbf{F} to find the partial derivatives in the sensitivities [28].

The input and output variables of the static power flow equation \mathbf{F} , \mathbf{w}_{PF} and \mathbf{z}_{PF} , respectively, needed to apply the implicit function theorem to compute the partial derivatives, are described in section 2.2. Fixed variables are considered as input variables and free variables as output variables. The partial derivatives of interest are included in the following matrix of partial derivatives and can be extracted to construct the sensitivities $\nabla \mathbf{h}$ [28]

$$\frac{\partial \mathbf{z}_{PF}}{\partial \mathbf{w}_{PF}} = - \left[\frac{\partial \mathbf{F}}{\partial \mathbf{z}_{PF}} \right]^{-1} \frac{\partial \mathbf{F}}{\partial \mathbf{w}_{PF}}. \quad (3.16)$$

The derivative of the power flow equations \mathbf{F} (2.14) with respect to its variables \mathbf{u} , \mathbf{p} , \mathbf{q} , and ψ at an operating point \mathbf{u}^* is given by expanding the result from [29] by the distributed slack approach as follows

$$\frac{\partial \mathbf{F}}{\partial (\mathbf{v}, \boldsymbol{\theta}, \mathbf{p}, \mathbf{q}, \psi)} = \begin{bmatrix} \langle \langle \text{diag}(\overline{\mathbf{Y}_{PF} \mathbf{u}^*}) \rangle \rangle + \langle \text{diag}(\mathbf{u}^*) \rangle \mathbf{N} \langle \mathbf{Y}_{PF} \rangle \mathbf{R}(\mathbf{u}^*) & -\mathbb{I}_b & \mathbf{0}_b & -\boldsymbol{\pi} \\ \mathbf{0}_b & -\mathbb{I}_b & \mathbf{0}_{b \times 1} & \end{bmatrix}. \quad (3.17)$$

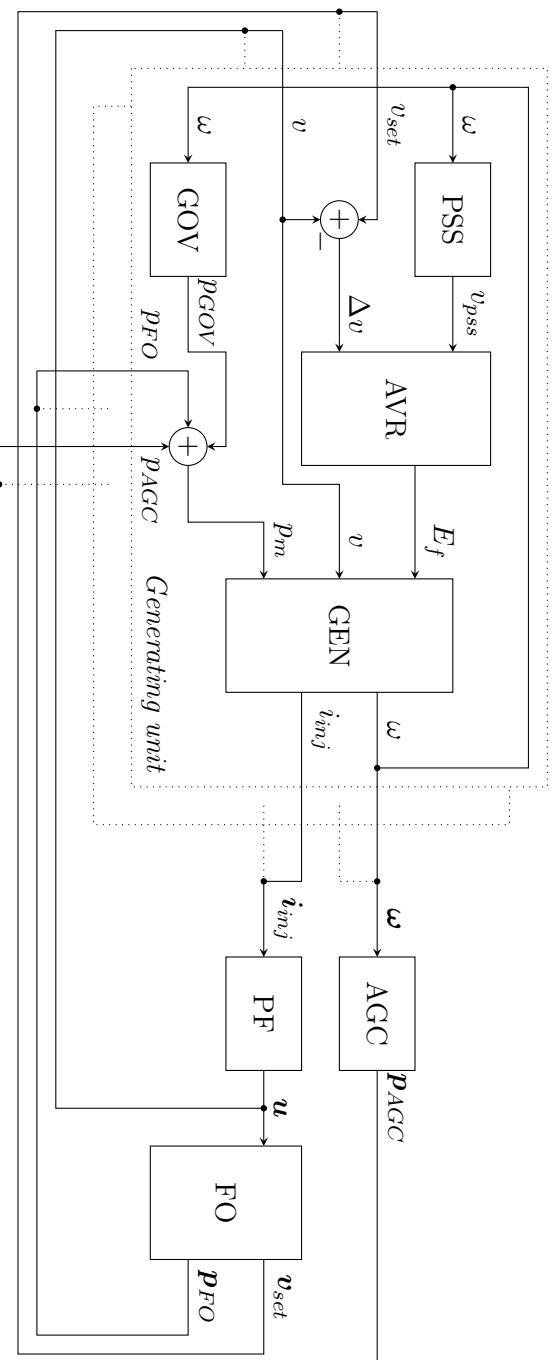


Figure 3.1: Block diagram of the dynamic power system simulator *DynPSSimPy* including the FO controller. The blocks PSS, AVR, GOV, GEN, AGC, PF and FO correspond to the power system stabilizer, the automated voltage regulator, the governor, the synchronous machine, the excitation system, the power flow equations and the FO controller, respectively. The blocks corresponding to one generating unit are grouped by the dotted frame, and possible additional generation units are indicated by the second dotted frame.

In the above equation the following expressions have been used to simplify the notation

$$\mathbf{N} = \begin{bmatrix} \mathbb{I}_b & \mathbf{0}_b \\ \mathbf{0}_b & -\mathbb{I}_b \end{bmatrix}, \quad (3.18a)$$

$$\langle \mathbf{A} \rangle = \begin{bmatrix} \text{Re}(\mathbf{A}) & -\text{Im}(\mathbf{A}) \\ \text{Im}(\mathbf{A}) & \text{Re}(\mathbf{A}) \end{bmatrix}, \quad (3.18b)$$

$$\mathbf{R}(\mathbf{u}) = \begin{bmatrix} \text{diag}(\cos \boldsymbol{\theta}) & -\text{diag}(\mathbf{v})\text{diag}(\sin \boldsymbol{\theta}) \\ \text{diag}(\sin \boldsymbol{\theta}) & \text{diag}(\mathbf{v})\text{diag}(\cos \boldsymbol{\theta}) \end{bmatrix}. \quad (3.18c)$$

Since the feedback of the controller brings some robustness against errors in the sensitivities $\nabla \mathbf{h}$, approximations thereof can be used. The presented computation of the sensitivities does not consider any information of the dynamic system models, only the static admittance matrix \mathbf{Y}_{PF} is used. This may introduce some deviations from the real sensitivities. However, the FO controller is robust enough against these discrepancies and does still converge, as will be shown in chapter 4.

3.3 Tuning of the Feedback Optimization Controller

The presented FO controller can be tuned by the step size α and the metric \mathbf{G} . Together they determine by how much the controller is allowed to change the input signal from the current input and thus how fast the controller is supposed to change the input signal from the current input to the optimal input determined with the QP (3.6) in every direction. If the current state of the system is not within the feasible area defined by the sets \mathcal{W} and \mathcal{Z} , the change of the input signal towards a feasible one is not limited by the step size α . As described, the constraint fulfilment of the output variables \mathbf{z} , given the new input signal \mathbf{w} , is checked by linearizing the expected system response of applying \mathbf{w} . This approximation can lead to temporary constraint violations if the step size α allows for big enough steps to operating points, in which the linearization of the system response is not accurate anymore.

Since the FO controller presented in the preceding sections is a discrete time controller, it comes with an additional tuning factor in form of the sampling time τ_{FO} . The step size α and metric \mathbf{G} should be chosen in a way, that allows the underlying system to change from one steady state to the next steady state within the duration of one sampling period τ_{FO} , before the next control input is applied. Formally speaking, this requires the dynamics of the physical system and the dynamics of the FO controller to act on sufficiently different timescales [13]. This concept allows estimating the step size limit and is presented in the following subsection.

3.3.1 Timescale Separation through Step Size Limit

To estimate the step size limit α_{max} , the results of [13], where the step size limit of a continuous time FO controller is derived, are applied to the FO setting used in this project. Although a discrete time controller is used, the continuous time theory can be used to estimate a (conservative) bound of the step size limit. For the sake of simplicity we fix the metric \mathbf{G} to equal identity, $\mathbf{G}(\mathbf{w}) = \mathbb{I}_l$. To determine the step size limit, it is necessary to find parameters that describe the steepness of the objective function Φ and the convergence of the physical system.

We assume that there exists a parameter $L > 0$ such that

$$\|\mathbf{H}(\mathbf{w})^T (\nabla \Phi(\mathbf{w}, \mathbf{g}(\mathbf{x}')) - \nabla \Phi(\mathbf{w}, \mathbf{g}(\mathbf{x})))\| \leq L \|\mathbf{x}' - \mathbf{x}\| \quad (3.19)$$

for all $\mathbf{x}', \mathbf{x} \in \mathbb{R}^n$, and for all $\mathbf{w} \in \mathbb{R}^m$. The parameter L describes the steepness of the objective function in the direction of \mathbf{z} . Note, that the objective function Φ needs to have compact level sets in the \mathbf{z} dimension in order to find a $L > 0$ and therefore to apply the results of [13].

To quantify the convergence of the physical system to a steady state, the concept of Lyapunov functions is used. Since the physical system is assumed to be stable and there exists a steady state map \mathbf{h} , there exists a Lyapunov function $W : \mathbb{R}^n \times \mathbb{R}^l \rightarrow \mathbb{R}$ such that for the parameters α, β, γ , and $\zeta > 0$

$$\alpha \|\mathbf{x} - \mathbf{h}(\mathbf{w})\|^2 \leq W(\mathbf{x}, \mathbf{w}) \leq \beta \|\mathbf{x} - \mathbf{h}(\mathbf{w})\|^2 \quad (3.20a)$$

$$\dot{W}(\mathbf{x}, \mathbf{w}) \leq -\gamma \|\mathbf{x} - \mathbf{h}(\mathbf{w})\|^2 \quad (3.20b)$$

$$\|\nabla_{\mathbf{w}} W(\mathbf{x}, \mathbf{w})\| \leq \zeta \|\mathbf{x} - \mathbf{h}(\mathbf{w})\|. \quad (3.20c)$$

Remark 3. The function \mathbf{f} describing the dynamics of the power system used in this project (2.21) is not continuous (see (2.31) or (2.34)). This contradicts [13, assumption II.1], which requires \mathbf{f} to be continuous. The assumption of \mathbf{f} being continuous in [13] is used to ensure the existence of a steady state map \mathbf{h} via the implicit function theorem. Despite this assumption not being satisfied, the results of [13] can be applied to this project, because \mathbf{f} describes the dynamics of a power system and the steady state map of a power system is given implicitly by the power flow equations (2.14).

With the necessary knowledge about the continuity of the objective function Φ through L and the convergence of the physical system through γ and ζ , the following theorem derived in [13] quantifies the step size limit α_{max} :

Theorem 2. *Given the parameters L, γ and ζ from the above equations, the step size limit α_{max} of a FO controller of the form (3.5) with $\mathbf{G} = \mathbb{I}_l$ is given by*

$$\alpha_{max} = \frac{\gamma}{\zeta L}. \quad (3.21)$$

Although the above theorem presents an easy way to compute the step size limit α_{max} , the therefore needed parameters are hard to compute. The analytic computation of L is impeded by the analytical computation of the Lipschitz constant $L_{\mathbf{g}}$ of \mathbf{g} and the computation of γ and ζ requires the knowledge of a Lyapunov function W , which is unknown for general power systems. The needed parameters can, however, be estimated by either fitting the parameters using an approximation of the Lyapunov function or by linearizing the nonlinear system (3.1). These two approaches are presented in the following paragraphs.

Parameter Fitting

The parameter L of the objective function Φ can be estimated using a set of random states $\{\mathbf{x}_{(1)}, \dots, \mathbf{x}_{(\nu)}\}$ and a set of random inputs $\{\mathbf{w}_{(1)}, \dots, \mathbf{w}_{(\nu)}\}$ to approximate the condition, that the relation (3.19) needs to hold for all $\mathbf{x}', \mathbf{x} \in \mathbb{R}^n$, and for all $\mathbf{w} \in \mathbb{R}^m$. The estimate of L is given by the most conservative option, that satisfies (3.19) for the set of random states and inputs

$$\hat{L} = \max \{L_{(1,1,1)}, \dots, L_{(\nu,\nu,\nu)}\}, \quad (3.22)$$

where the parameters $L_{(i,j,k)}$ for $(i, j, k) \in \{[1, \nu]^3, i \neq j\}$ are given by

$$L_{(i,j,k)} = \frac{\|\mathbf{H}(\mathbf{w}_{(k)})^T (\nabla \Phi(\mathbf{w}_{(k)}, \mathbf{g}(\mathbf{x}_{(i)})) - \nabla \Phi(\mathbf{w}_{(k)}, \mathbf{g}(\mathbf{x}_{(j)})))\|}{\|\mathbf{x}_{(i)} - \mathbf{x}_{(j)}\|}. \quad (3.23)$$

Similarly, using an approximation of the Lyapunov function \tilde{W} , the parameters γ and ζ can be estimated

$$\hat{\gamma} = \max \{\gamma_{(1)}, \dots, \gamma_{(\nu)}\} \quad (3.24a)$$

$$\hat{\zeta} = \max \{\zeta_{(1)}, \dots, \zeta_{(\nu)}\}, \quad (3.24b)$$

where the parameters $\gamma_{(i)}$ and $\zeta_{(i)}$ for $i \in [1, \nu]$ are given by

$$\gamma_{(i)} = -\frac{\dot{\tilde{W}}(\mathbf{x}_{(i)}, \mathbf{w}_{(i)})}{\|\mathbf{x}_{(i)} - \mathbf{h}(\mathbf{w}_{(i)})\|^2} \quad (3.25a)$$

$$\zeta_{(i)} = \frac{\|\nabla_{\mathbf{w}} \tilde{W}(\mathbf{x}_{(i)}, \mathbf{w}_{(i)})\|}{\|\mathbf{x}_{(i)} - \mathbf{h}(\mathbf{w}_{(i)})\|}. \quad (3.25b)$$

As approximation of the Lyapunov function \tilde{W} , the distance between the current states \mathbf{x} and the steady states of that input \mathbf{w} given by the steady state map $\hat{\mathbf{h}}$ is proposed

$$\tilde{W}(\mathbf{x}, \mathbf{w}) = \left\| \mathbf{x} - \hat{\mathbf{h}}(\mathbf{w}) \right\|. \quad (3.26)$$

The quality of this approximation of the real Lyapunov function W will be discussed in section 4.2.3 together with the results of the step size limit estimate $\hat{\alpha}_{max}$ based on the methodology presented in this paragraph.

Linearization

The second approach to estimate the parameters used to compute the step size limit, is to approximate the nonlinear system (3.1) by a linearization thereof around an operating point $(\mathbf{x}_{(i)}, \mathbf{w}_{(i)})$ of the form

$$\dot{\mathbf{x}} \approx \mathbf{A}_{(i)}\mathbf{x} + \mathbf{B}_{(i)}\mathbf{w} \quad (3.27a)$$

$$\mathbf{z} \approx \mathbf{C}_{(i)}\mathbf{x}, \quad (3.27b)$$

where the system matrices $\mathbf{A}_{(i)} \in \mathbb{R}^{n \times n}$, $\mathbf{B}_{(i)} \in \mathbb{R}^{n \times l}$ and $\mathbf{C}_{(i)} \in \mathbb{R}^{m \times n}$ are defined as follows

$$\mathbf{A}_{(i)} = \nabla_{\mathbf{x}} \mathbf{f}|_{\mathbf{x}=\mathbf{x}_{(i)}} \quad (3.28a)$$

$$\mathbf{B}_{(i)} = \nabla_{\mathbf{w}} \mathbf{f}|_{\mathbf{w}=\mathbf{w}_{(i)}} \quad (3.28b)$$

$$\mathbf{C}_{(i)} = \nabla_{\mathbf{x}} \mathbf{g}|_{\mathbf{x}=\mathbf{x}_{(i)}}. \quad (3.28c)$$

By using the objective function shown in equation (3.10), the equation in (3.19) simplifies in the case of the linearized system to

$$2\|\nabla \mathbf{h}^T \mathbf{Q}_z \mathbf{C}_{(i)}\| \cdot \|\mathbf{x}' - \mathbf{x}\| \leq L_{(i)} \|\mathbf{x}' - \mathbf{x}\|. \quad (3.29)$$

This yields the parameter $L_{(i)} = 2\|\nabla \mathbf{h}^T \mathbf{Q}_z \mathbf{C}_{(i)}\|$.

For a linear system as in equations (3.27), $W(\mathbf{x}, \mathbf{w}) = \|\mathbf{x} - \mathbf{h}(\mathbf{w})\|_{\mathbf{P}_{(i)}}^2$ is a Lyapunov function, where $\mathbf{P}_{(i)} \in \mathbb{S}_+^n$ satisfies the Lyapunov equation

$$\mathbf{A}_{(i)}^T \mathbf{P}_{(i)} + \mathbf{P}_{(i)} \mathbf{A}_{(i)} = -\mathbf{Q}_{(i)}, \quad (3.30)$$

for any $\mathbf{Q}_{(i)} \in \mathbb{S}_+^n$. The parameters $\gamma_{(i)}$ and $\zeta_{(i)}$ for the operating point $(\mathbf{x}_{(i)}, \mathbf{w}_{(i)})$ can be computed analytically in the case of the linearized system and result to

$$\gamma_{(i)} = \lambda_{\mathbf{Q}_{(i)}}^{min} \quad (3.31a)$$

$$\zeta_{(i)} = \left\| \mathbf{P}_{(i)} \mathbf{A}_{(i)}^{-1} \mathbf{B}_{(i)} \right\|, \quad (3.31b)$$

where $\lambda_{\mathbf{Q}_{(i)}}^{min}$ is the smallest eigenvalue of $\mathbf{Q}_{(i)}$.

The estimate of the step size limit $\hat{\alpha}_{max}$ in the linearization method is given by the most conservative step size limit $\alpha_{max,(i)}$ of all considered operating points $\{(\mathbf{x}_{(1)}, \mathbf{w}_{(1)}), \dots, (\mathbf{x}_{(\nu)}, \mathbf{w}_{(\nu)})\}$

$$\hat{\alpha}_{max} = \min \{ \alpha_{max,(1)}, \dots, \alpha_{max,(\nu)} \}, \quad (3.32)$$

where the step size limits of the operating points $\alpha_{max,(i)}$ are evaluated by plugging the parameters $L_{(i)}, \gamma_{(i)}$ and $\zeta_{(i)}$ into equation (3.21).

Remark 4. This method of estimating the step size limit via a linearization of the nonlinear system requires a solution of the Lyapunov equation (3.30). According to Lyapunov's theorem [30], there exists a unique $\mathbf{P}_{(i)} \in \mathbb{S}_+^n$ satisfying equation (3.30) for any $\mathbf{Q}_{(i)} \in \mathbb{S}_+^n$ if the linearized system defined by the matrix $\mathbf{A}_{(i)}$ is asymptotically stable. Further, the operating point $(\mathbf{x}_{(i)}, \mathbf{w}_{(i)})$ is asymptotically stable, if the linearization $\mathbf{A}_{(i)}$ of the nonlinear system (3.1) at that point is asymptotically stable.

The used power system turns out to have a marginally stable mode corresponding to a reference point for the rotor angles $\boldsymbol{\delta}$ of the synchronous machines in the system, and therefore there does not exist a unique $\mathbf{P}_{(i)} \in \mathbb{S}_+^n$ according to equation (3.30). Since the angle reference for the rotor angles does not influence the system dynamics, this marginally stable mode can be isolated and removed from $\mathbf{A}_{(i)}$ by choosing an appropriate transform of coordinates.

Let's define an angle reference corresponding to the average rotor angle $\bar{\delta}$. The new state coordinates $\tilde{\mathbf{x}}$ are then given by

$$\tilde{\mathbf{x}} = \mathbf{U}^T \mathbf{x}, \quad (3.33)$$

where $\mathbf{U} \in \mathbb{R}^{n \times n}$ is a unitary matrix given by the singular value decomposition of the positive definite matrix $\boldsymbol{\Omega} \in \mathbb{R}_+^{n \times n}$, $\boldsymbol{\Omega} = \mathbf{U} \boldsymbol{\Sigma} \mathbf{U}^T$. The matrix $\boldsymbol{\Omega}$ is chosen such that the average rotor angle $\bar{\delta}$ is subtracted from every rotor angle and all other states stay untouched when multiplying $\boldsymbol{\Omega}$ with the state vector \mathbf{x}

$$\boldsymbol{\Omega} = \mathbb{I}_n - \mathbf{U} \boldsymbol{\delta} \mathbf{U}_\delta^T, \quad (3.34)$$

where $\mathbf{U}_\delta \in \mathbb{R}^n$ is a vector containing $1/g$ at each entry corresponding to a state being a rotor angle and 0 otherwise, with g being the number of synchronous machines in the power system and thus rotor angles in the state vector.

This coordinate transform leads to the following transformed linearized system

$$\dot{\tilde{\mathbf{x}}} \approx \underbrace{\mathbf{U}^T \mathbf{A}_{(i)} \mathbf{U}}_{\tilde{\mathbf{A}}_{(i)}} \tilde{\mathbf{x}} + \underbrace{\mathbf{U}^T \mathbf{B}_{(i)}}_{\tilde{\mathbf{B}}_{(i)}} \mathbf{w} \quad (3.35a)$$

$$\mathbf{z} \approx \underbrace{\mathbf{C}_{(i)} \mathbf{U}}_{\tilde{\mathbf{C}}_{(i)}} \tilde{\mathbf{x}}. \quad (3.35b)$$

Due to the choice of coordinate transform, the new state vector $\tilde{\mathbf{x}}$ will include a state corresponding to the rotor angle reference with zero dynamics as shown in the following equation

$$\tilde{\mathbf{A}}_{(i)} = \begin{bmatrix} \mathbf{0}_{n \times 1} & \tilde{\mathbf{a}}_{(i)} \\ & \hat{\mathbf{A}}_{(i)} \end{bmatrix}, \quad (3.36)$$

where $\hat{\mathbf{A}}_{(i)} \in \mathbb{R}_{(n-1) \times (n-1)}$ and $\tilde{\mathbf{a}}_{(i)} \in \mathbb{R}_{1 \times (n-1)}$.

To estimate the step size limit α_{max} with the linearization of the nonlinear system, this state is omitted and thus the matrices $\hat{\mathbf{A}}_{(i)}, \hat{\mathbf{B}}_{(i)}$, and $\hat{\mathbf{C}}_{(i)}$, where the rows and columns corresponding to this state have been removed, are used in the computation of $\hat{\alpha}_{max}$ with the linearization method.

Chapter 4

Simulation Environment & Results

After elaborating the theoretical framework of controlling a power system including its dynamics with a FO controller in the previous chapters, this chapter presents the simulation results. The first section introduces the simulation set-up and the optimal power flow (OPF) controller used to benchmark the FO controller. Section 4.2 then presents and discusses the main simulation results by first showing the working principle of the FO controller at an economic dispatch example in section 4.2.1, and then moving to emergency operation in section 4.2.2. Finally, the stability and robustness of the FO controller is discussed in sections 4.2.3 and 4.2.4, respectively.

4.1 Simulation Environment

Before moving to the simulation results, the environment, in which the FO controller is tested, is presented. The simulations are performed with the dynamic power system simulator *DynPSSimPy* introduced in chapter 2 on the IEEE 39 bus system. Therefore, the ODE (2.21) are integrated with a temporal resolution of $\tau_I = 0.01$ s. The IEEE 39 bus system is used commonly to implement and test new concepts and was introduced in [31]. The test network comprises 34 lines, 12 transformers and 10 generators. Generator 1 at bus 39 thereof represents an aggregation of a bigger power system with multiple generators, however this only changes the parameters of the synchronous machine model. The system is operated at a voltage level of 345 kV and a frequency of 60 Hz. The topology is shown in the single line diagram in figure 4.1 and the technical data of the network is based on [17] and shown in appendix A. During the simulations, power withdrawals of loads and power injections of uncontrolled generation are kept constant.

4.1.1 Feedback Optimization Controller

A FO controller as described in chapter 3 is used to control the test system. To prevent generators from overloading, the active power generation set points \mathbf{p}_{set} are limited to be within 0 and 1 p.u. The voltage set points of the synchronous machines \mathbf{v}_{set} are limited to values between 0.9 and 1.1 p.u. This leads to the following matrix $\mathbf{D}_{\mathbf{w}}$ and operating limits $\mathbf{e}_{\mathbf{w},min}$ and $\mathbf{e}_{\mathbf{w},max}$ for the input variables \mathbf{w} , which define the set of admissible inputs \mathcal{W} according to equation (3.11)

$$\mathbf{D}_{\mathbf{w}} = \mathbb{I}_{2g}, \quad \mathbf{e}_{\mathbf{w},min} = \begin{bmatrix} \mathbf{0}_{g \times 1} \\ 0.9 \cdot \mathbf{1}_{g \times 1} \end{bmatrix}, \quad \mathbf{e}_{\mathbf{w},max} = \begin{bmatrix} \mathbf{1}_{g \times 1} \\ 1.1 \cdot \mathbf{1}_{g \times 1} \end{bmatrix}. \quad (4.1)$$

The output variables \mathbf{z} are constrained to prevent the voltage from collapsing and transmission lines and transformers from overloading. Therefore the bus voltage magnitude \mathbf{v} is limited to the range of [0.9, 1.1] p.u. Instead of putting a limit on the current magnitudes of the branches $|\mathbf{i}_{ij}|$, the absolute value of the voltage magnitude and angle differences across transmission lines and transformers are limited to $|\Delta \mathbf{v}| \leq 0.08$ and $|\Delta \boldsymbol{\theta}| \leq 0.3$, respectively. This will bound the

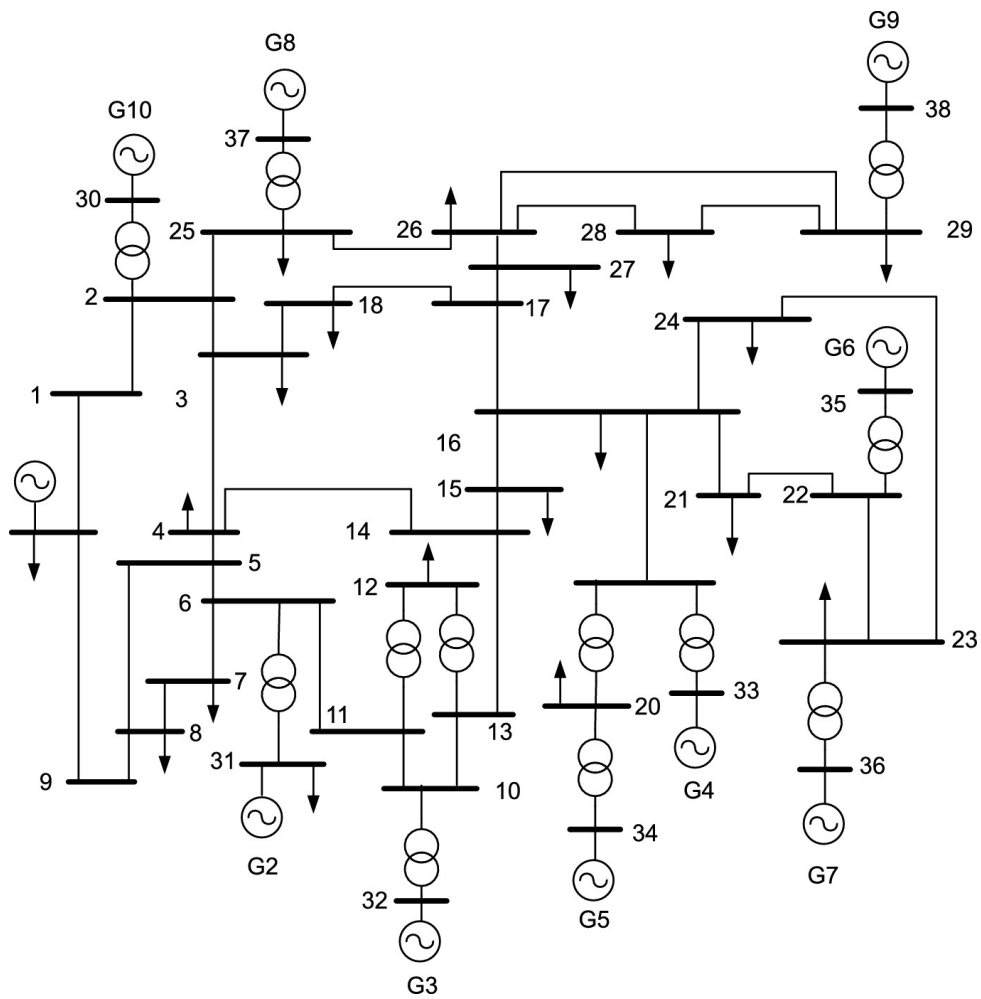


Figure 4.1: Single line diagram of IEEE 39 bus system [32]. Generator 1, located at bus 39 at the very left of the diagram (this bus and generator are not labelled in the figure), represents an aggregation of a bigger power system with multiple generators.

currents on these elements. Furthermore, it reduces the nonlinear current limits to linear constraints and will ensure that the voltage angle and magnitude difference and thus also the current limit on branches won't be exceeded in case of the disconnection of a branch and the subsequent re-closure thereof. The constraint matrix \mathbf{D}_z and the bounds $\mathbf{e}_{z,min}$, $\mathbf{e}_{z,max}$ are given as follows

$$\mathbf{D}_z = \begin{bmatrix} \mathbb{I}_g & \\ \mathbf{\Delta}_b & \mathbf{\Delta}_b \end{bmatrix}, \quad \mathbf{e}_{z,min} = \begin{bmatrix} 0.9 \cdot \mathbb{1}_{b \times 1} \\ \mathbf{0}_{2n_b \times 1} \\ \mathbf{0}_{2n_b \times 1} \end{bmatrix}, \quad \mathbf{e}_{z,max} = \begin{bmatrix} 1.1 \cdot \mathbb{1}_{b \times 1} \\ 0.08 \cdot \mathbb{1}_{2n_b \times 1} \\ 0.3 \cdot \mathbb{1}_{2n_b \times 1} \end{bmatrix}, \quad (4.2)$$

where $\mathbf{\Delta}_b = [\mathbf{\Delta}_b'^T \quad -\mathbf{\Delta}_b'^T]^T$ is given by the matrix $\mathbf{\Delta}_b' \in \{-1, 0, 1\}^{n_b \times b}$ and n_b is the number of branches. The entry of $\mathbf{\Delta}_b'$ in the i th column and j th row is 1 if the branch corresponding to the i th column departs from bus j , -1 if it goes to bus j and 0 otherwise.

The FO controller is tuned with a step size of $\alpha = 3 \times 10^{-5}$, and the identity matrix as metric \mathbf{G} : $\mathbf{G}(\mathbf{w}) = \mathbb{I}_{2g}$. This allows to apply theorem 2 when looking at the stability of the FO controller in section 4.2.3. The used cost function Φ is dependent of the application and will therefore be introduced in the sections below. The FO controller is run with a sampling time of $\tau_{FO} = 5$ s. Unless stated other, the sensitivities $\nabla \mathbf{h}$ are updated each time the control signal is updated by using the current system voltages \mathbf{u} as operating point \mathbf{u}^* (see section 3.2.1) and the actual system topology. The optimization problem (3.6) is solved using the symbolic framework *CasADi* [33] and the optimization software package *Ipopt* [26].

4.1.2 Optimal Power Flow Controller as a Benchmark

To compare the performance of the FO controller, an OPF controller is implemented as a benchmark. The control input of the OPF is obtained by solving the following optimization problem [4]

$$\min_{\mathbf{w}, \mathbf{z}} \quad \Phi(\mathbf{w}, \mathbf{z}) \quad (4.3a)$$

$$\text{s.t. } \mathbf{F}(\mathbf{u}, \mathbf{p}, \mathbf{q}, 0) = 0 \quad (4.3b)$$

$$\mathbf{w} \in \mathcal{W} \quad (4.3c)$$

$$\mathbf{z} \in \mathcal{Z}. \quad (4.3d)$$

Note, that the power flow equations \mathbf{F} are enforced explicitly by adding them as constraints to the above optimization problem (4.3b) and not using feedback of the physical system. The variables \mathbf{u} , \mathbf{p} and \mathbf{q} are given according to section 2.2.1 and the mismatch ψ is set to zero, since the AGC should not need to act after the optimal control inputs \mathbf{w}^* are applied. Enforcing the power flow equations explicitly makes the OPF less robust to model uncertainty and adds computational complexity to the above optimization problem compared to the QP (3.6), that needs to be solved in the FO process. To make the simulation results of the OPF controller comparable to the ones of the FO controller, the same cost function Φ and sets \mathcal{W} and \mathcal{Z} are used.

The input variables solving the optimization problem (4.3), \mathbf{w}^* , are computed using the already introduced software packages *CasADi* [33] and *Ipopt* [26]. After computing them, the input variables are applied to the dynamic power system model by ramping the active power and voltage set points of the generators in n_{OPF} steps from their current value to the computed input values \mathbf{w}^* , where every τ_{OPF} seconds a step is taken. In this benchmark set-up, a ramp with 10 steps $n_{OPF} = 10$, and the same time step as for the FO controller $\tau_{OPF} = \tau_{FO}$ is used to keep the system stable. Recomputing the input values \mathbf{w}^* is necessary only when parameters of the controller (cost function or the constraints), or the power system (topology, consumption, or uncontrolled generation) are changed. Since the OPF described in equations (4.3) does not

take into account any power system dynamics, the optimal control inputs \mathbf{w}^* will not consider any dynamics. Consequently, there is no guarantee, that the constraints are satisfied during the transients states when applying the control inputs \mathbf{w}^* , and no certificate for stability.

Remark 5. To ensure the N-1 criteria and that the operating limits are satisfied in each contingency case, the OPF optimization problem (4.3) can be extended. For each contingency case (i.e., each branch tripping), an additional set of power flow constraints, resulting from a power system model without the branch considered as tripped in this contingency case, and output constraints, for the output variables valid in this contingency case, can be added. The resulting optimization problem is called *security constrained OPF* [4]. Since the additional security constraints are based on a power system model, the robustness against model inaccuracies would be lost when implementing the same approach on a FO controller. Furthermore, the computational effort would increase substantially. The result of a security constrained OPF can, however, be approximated by adding security margins to the operating limits.

4.2 Simulation Results

4.2.1 Working Principles of Controllers

The above described FO and OPF controllers are first applied to an economic dispatch problem to demonstrate their working principles. For that reason, the costs function Φ is chosen to put a quadratic cost on the active power set point of each generator. The first half of the generators (i.e., generators 1 - 5) are penalized with double the cost of the second half of the generators

$$\Phi = \sum_{i=1}^5 (600 \cdot p_{set,i}^2 + 200 \cdot p_{set,i}) + \sum_{i=6}^{10} (300 \cdot p_{set,i}^2 + 100 \cdot p_{set,i}). \quad (4.4)$$

No cost is put on the voltage set point and on the output variables \mathbf{z} .

The active power generation set points of the generating units \mathbf{p}_{set} in the test system at the starting point of the simulation are according to the starting point \mathbf{w}_0 as defined in table A.4. The initial states \mathbf{x}_0 result from equation (2.22) based on \mathbf{w}_0 . Both controllers are used to minimize the objective function defined by the parameters in equation (4.4). The simulated operating costs along with the theoretic steady state optimal operating cost computed by the optimization problem (4.3) are shown in figure 4.2. The input and output variables of the FO and OPF simulation can be seen in figure 4.4. The power system controlled by the OPF controller is driven in the specified $n_{OPF} = 10$ steps to the optimal operating point. Since assumptions 1 and 2 hold, and the step size α is chosen small enough (i.e., such that $\alpha < \alpha_{max}$ is satisfied), the power system controlled by the FO controller converges to a stable equilibrium, with a higher operating cost. This difference in performance will be discussed in the following paragraphs.

The requirement of choosing a small enough step size α can be explained when looking at figure 4.3. It shows the active power set points and generator speeds during the first seconds of the economic dispatch simulation with the FO controller. The changes in active power generation set point made by the FO controller at $t = 10, 15, 20, \dots$ s are clearly recognizable. In between these steps, a slight change in the set points is visible. These smaller changes between the adjustments of the FO controller are introduced by the governors and the AGC (primary and secondary frequency control), which react to the small power imbalances and thus frequency deviations created by the FO controller when redispatching the generation between the machines. The steps at $t = 10, 15, 20, \dots$ s are taken after the transient triggered by the change in control signal has diminished. Tuning the FO controller with a smaller sampling time or bigger step size, might lead to a change in control signal before the system has settled and thus could turn the system unstable.

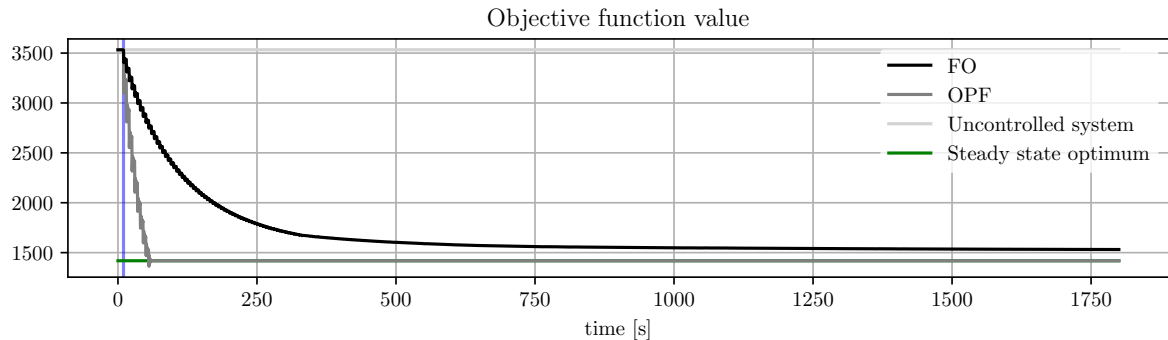


Figure 4.2: Objective function value of the economic dispatch simulation for the FO and OPF controllers, the uncontrolled system and the steady state optimum. The vertical blue line marks the starting point of the controllers.

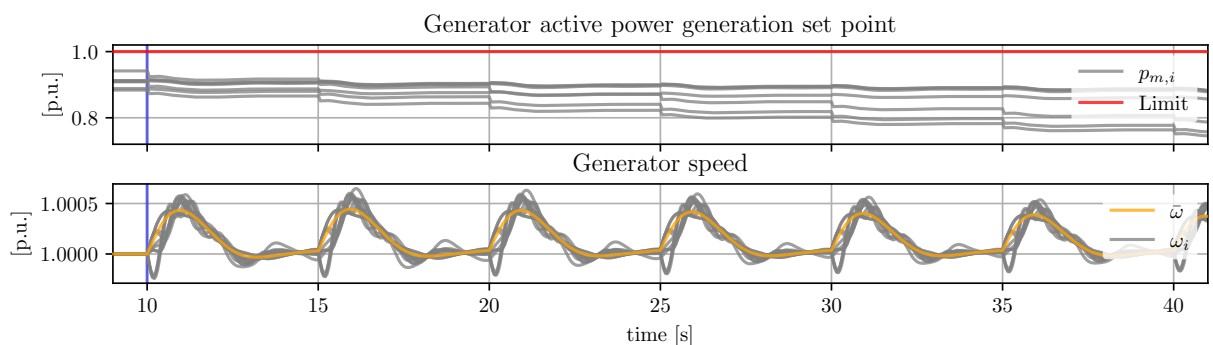
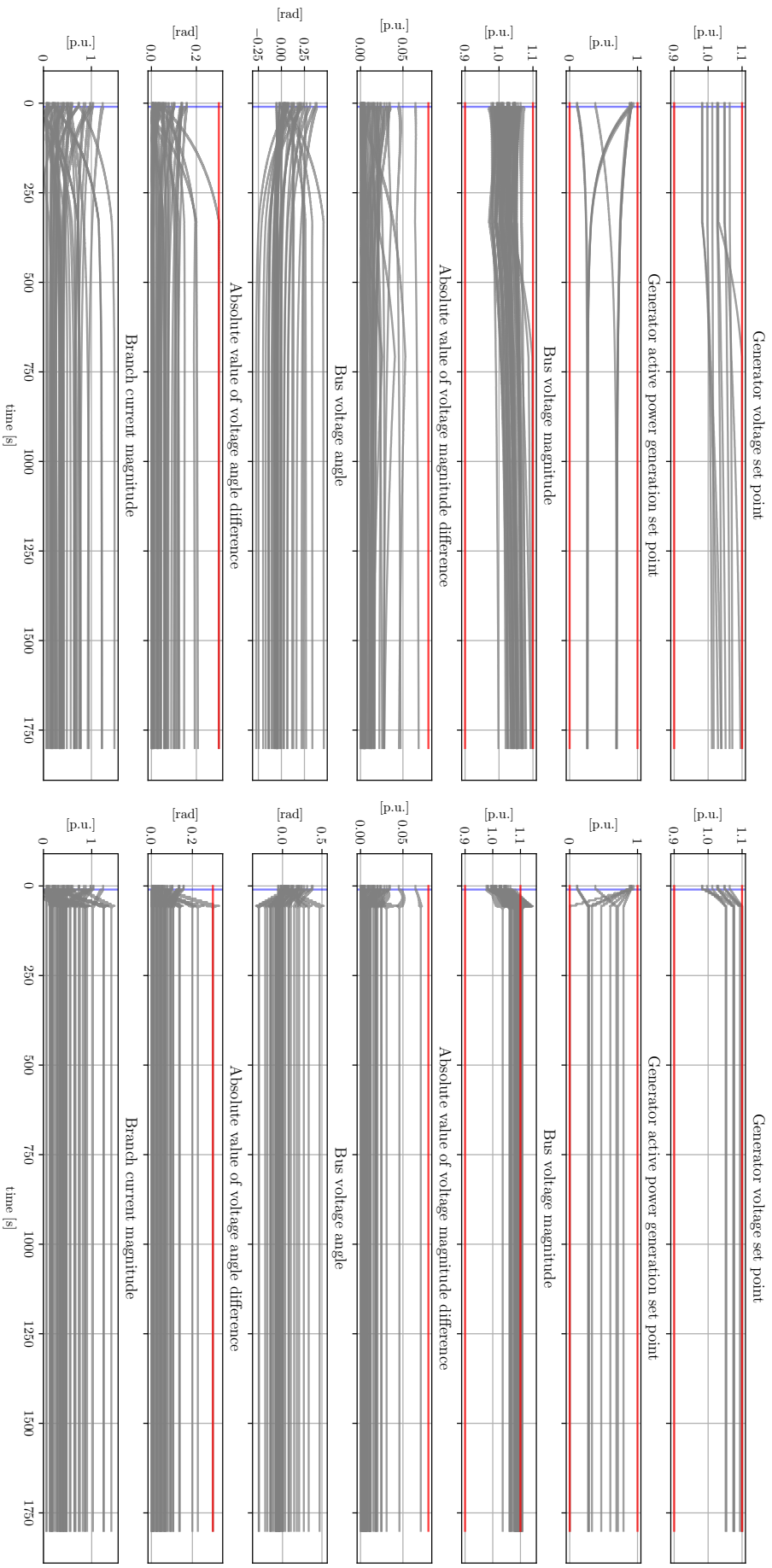


Figure 4.3: Upper panel: Active power generation set point during the first seconds of the economic dispatch simulation with the FO controller. The vertical red line shows the operating limit.

Lower panel: Generator speed during the first seconds of the economic dispatch simulation with the FO controller. The orange line depicts the average system frequency $\bar{\omega}$.

The power system controlled by the OPF does violate certain constraints like the bus voltage magnitude v and the bus voltage angle difference $\Delta\theta$ during its transient, as can be seen in figure 4.4b. Moreover, not only during transients but also at steady state, the voltage magnitude constraint is violated. That results from the excitation system of type *SEXS*. This excitation system does not have an integral part and therefore can give rise to a steady state error between the voltage magnitude set points v_{set} and the bus voltage magnitudes v at generator-buses. This model imperfection is not considered in the power system model used to compute the OPF control signal. Since the OPF controller has no feedback loop, the steady state error is not recognized and therefore not corrected by the OPF controller. The FO controller, in contrast, does correct for this model imperfection of the excitation system. If disturbances like a change in load power or disconnecting a transmission line were introduced to the power system, the constraint violation of the power system controlled by the OPF could even increase, whereas the FO controller is expected to further on meet the operating constraints.

The constraint violations of the OPF controller is one reason for the power system controlled by the OPF controller to result in a lower objective value than the power system controlled by the FO controller. A further reason is the used sensitivities $\nabla\mathbf{h}$ in the FO controller, which are computed as described in section 3.2.1. As mentioned above, the excitation system of the dynamic power system model does differ from an ideal excitation system as assumed in the static power flow equations. Therefore the computed sensitivities have some inaccuracies. The



(a) FO controller.

(b) OPF controller.

Figure 4.4: Input and output variables of the power system in the economic dispatch simulation for the FO and OPF controllers, with their constraints indicated by the horizontal red lines. The vertical blue line marks the starting point of the controllers.

mismatch between the used sensitivities and the real sensitivities leads the FO controller to converge to a suboptimal operating point.

Compared to the FO controller, the OPF has the advantage of knowing the optimal operating point a priori, which allows to reach (or get close to) this operating point faster (by taking the risk of violating operation limits during the transient and the risk of destabilizing the power system by applying a too big step-change in the control signal to the power system). In situations, where an initialization of the controller is required (e.g., after activating the controller, changing the objective function or constraints, or a big disturbance) like in this test case, this results in a faster convergence of the OPF controller compared to the FO. This advantage of the OPF controller could be exploited to speed up the convergence of the FO controller, if a model and the corresponding data is available. A control input computed using the OPF controller could be applied to the power system before controlling it with the FO controller. In doing so, the initialization phase is speeded up, while ensuring that the operating constraints are satisfied asymptotically. To reduce possible constraint violations before switching from OPF to FO, which could occur due to model mismatch, security margins can be added to the operating limits of the OPF controller.

When looking at the development of the variables of the power system controlled by the FO controller in figure 4.4a, a discontinuity in their slope at $t \approx 300$ s is visible (especially the voltage set points \mathbf{v}_{set}). At this point, the controller has to change the direction, because the voltage angle difference is hitting the limit. The control law of the FO controller given in equation (3.5) chooses the next control signal by projecting the direction determined by $\mathbf{G}^{-1}(\mathbf{w})\nabla\Phi(\mathbf{w}, \mathbf{h}(\mathbf{w}))$ to a linearization of the feasible set. Therefore, the direction is adjusted when approaching operating limits in order not to violate them.

4.2.2 Control in Emergency Operation

In this example, the controllers are applied to control the IEEE 39 bus system in an emergency mode. Again, the same starting point $(\mathbf{x}_0, \mathbf{w}_0)$ as in the previous example is used for this simulation. At $t = 10$ s, the transmission line L23-24 connecting buses B23 and B24 trips. This leads to increased current magnitudes on other branches. Depending on the thermal limits of the remaining branches, they could trip as well, leading to cascading outages. We assume that no branch trips due to overloading, but the increased currents put the power system in emergency operation mode. This allows us to test the performance of the controllers. To reduce the currents on the branches, the system operators aim to reconnect the tripped transmission line and turn on the controller at $t = 40$ s, which allows reconnecting the line at $t = 120$ s. In order to enable the reclosure of the transmission line and minimize transients after reclosure, the objective of the controller is defined to reduce the voltage difference between buses B23 and B24 $|u_{23} - u_{24}|^2$. Therefore, a high cost is put on the voltage magnitude and voltage angle difference of these buses

$$\Phi = 10^5 \cdot [(v_{23} - v_{24})^2 + (\theta_{23} - \theta_{24})^2]. \quad (4.5)$$

No cost is put on the input variables \mathbf{w} in this application.

The voltage difference between buses B23 and B24 over time is shown in figure 4.5 for both controllers, the uncontrolled system, and the steady state optimum. The currents on the branches for the controlled and uncontrolled systems are shown in figure 4.7, and the input and output variables of the FO and OPF simulation can be seen in figure 4.6. During the simulation, the power system model used to compute the sensitivities for the FO controller and the power flow equations for the OPF controller is updated for both controllers after the line trips.

Both controllers succeed in reducing the voltage difference between buses B23 and B24, that were connected by the tripped transmission line. With that also the loading on the highly loaded equipment is reduced in reasonable time. Temporarily, the system controlled by the FO violates

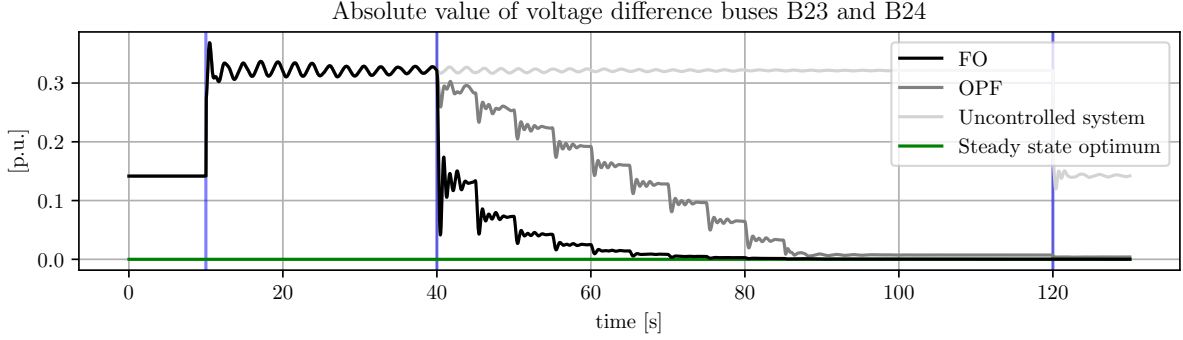


Figure 4.5: Voltage difference of buses B23 and B24 in the emergency operation simulation for the FO and OPF controllers, the uncontrolled system and the steady state optimum. The vertical blue lines mark the disconnection of line L23-24, the starting point of the controllers and the reclosure of line L23-24, respectively.

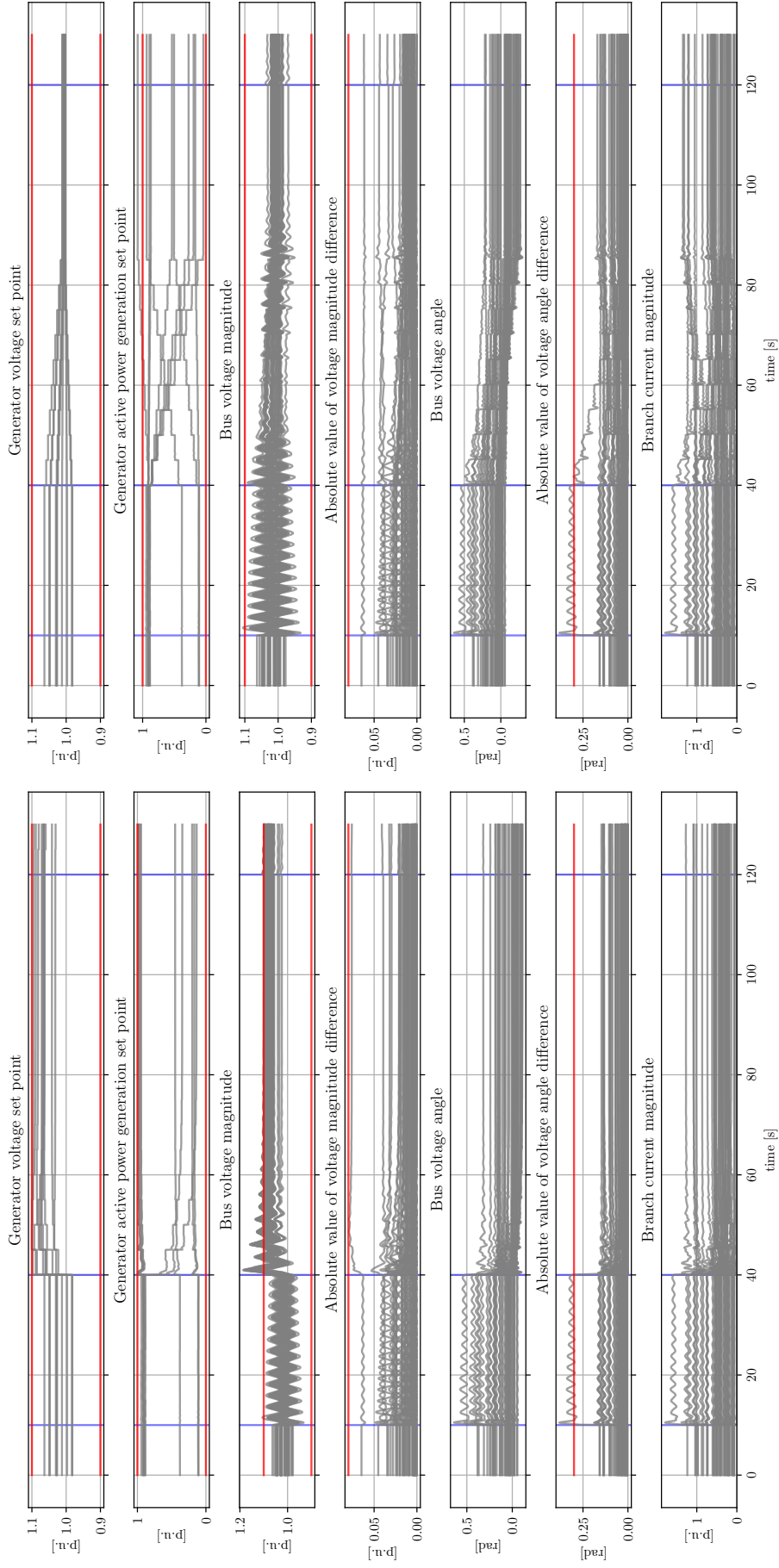
the bus voltage magnitude constraints, as can be seen in figure 4.6a. Compared to the OPF controller, the FO controller is able to reach a lower voltage difference. Due to the possible steady state error of the bus voltage magnitude because of the excitation system *SEXS*, the excitation system is again responsible for the performance difference of the controllers. Since the OPF controller has no feedback loop, the steady state error of the bus voltage magnitudes hinders the system to reach the operating point determined by the OPF by applying the computed optimal set points to the generators. In contrast, the feedback and the integral part of the FO controller allow correcting for this steady state error. In this example the FO controller is robust enough to converge to the optimal solution, despite the inaccuracies in the sensitivities introduced by the excitation system.

As can be seen in figure 4.6, the voltage angle difference constraint is violated the moment the controllers are turned on at $t = 40$ s. Due to the definition of the control law of the FO controller, it reacts to that by driving the system to a feasible operating point in one step. The constraint violation allows the FO controller to take a step, that is not limited by the step size α . Therefore, the voltage angle difference constraint reduces the duration, in which the system is under high loading conditions. However, normal operating constraints might lead to infeasibility during emergency operation and thus violate assumption 1. A possible reason for that could be the loss of a highly loaded branch. After this element trips, the normal operating limits can not be met anymore by any operating point, because the missing element leads to overloading of other elements. A possible solution to infeasible problems is sketched in remark 2.

4.2.3 Stability of Feedback Optimization Controller

To ensure stability of the power system controlled by the FO controller, theorem 1, that ensures convergence of the FO controller, together with the step size limit of theorem 2 are applied to the emergency operation set-up described in the previous section. The step size limit α_{max} is estimated using the parameter fitting and the linearization methods presented in section 3.3.1.

To estimate the step size limit α_{max} with the parameter fitting method, a set of random states $\{\mathbf{x}_{(1)}, \dots, \mathbf{x}_{(\nu)}\}$ and random inputs $\{\mathbf{w}_{(1)}, \dots, \mathbf{w}_{(\nu)}\}$ is needed. This set is built by sampling $\nu = 50$ converging state-input-combinations from a multivariate normal distribution with the initial state \mathbf{x}_0 and input \mathbf{w}_0 as mean vector, and a standard deviation of 0.01 for all



(a) FO controller.

(b) OPF controller.

Figure 4.6: Input and output variables of the power system in the emergency operation simulation for the FO and OPF controllers, with their constraints indicated by the horizontal red lines. The vertical blue lines mark the disconnection of line L23-24, the starting point of the controllers and the reclosure of line L23-24, respectively.

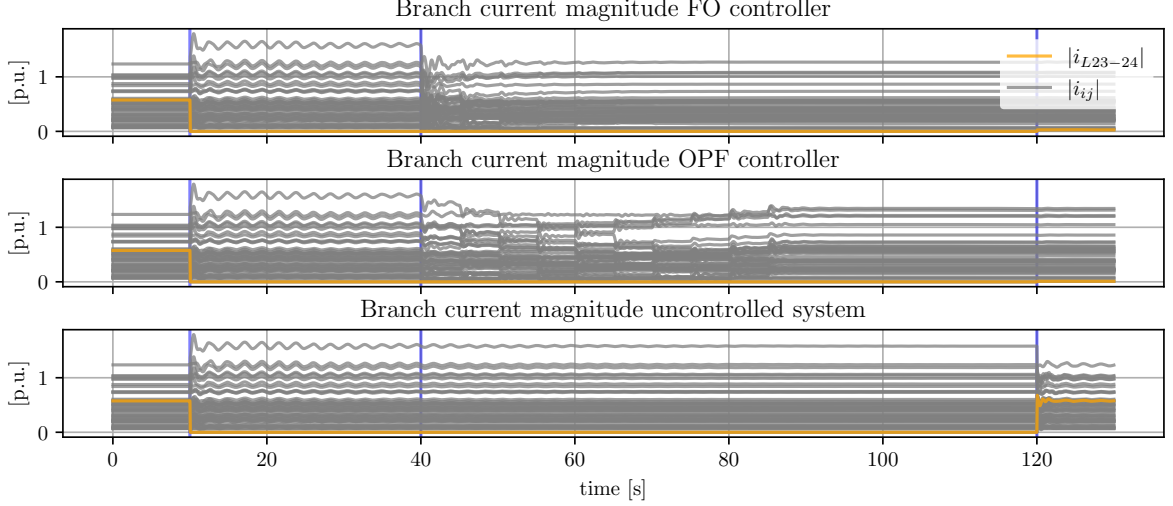


Figure 4.7: Branch currents magnitudes in the emergency operation simulation. Line L23-24 is highlighted in orange. The vertical blue lines mark the disconnection of line L23-24, the starting point of the controllers and the reclosure of line L23-24, respectively.

states, 0.1 for the active power set points and 0.03 for the voltage set points

$$\mathcal{N} \left(\begin{bmatrix} \mathbf{x}_0 \\ \mathbf{w}_0 \end{bmatrix}, \begin{bmatrix} 0.01^2 \cdot \mathbb{I}_n & & \\ & 0.1^2 \cdot \mathbb{I}_g & \\ & & 0.03^2 \cdot \mathbb{I}_g \end{bmatrix} \right). \quad (4.6)$$

The set of operating points used for the linearization method is extracted by the above derived sets of random states and inputs: $(\mathbf{x}_{(i)}, \mathbf{w}_{(i)})$ for $i = 1 \dots 50$. Additionally to those random operating points, the operating points during the simulation of the emergency operation example are used to estimate the step size limit with the linearization method. The resulting step size limit estimates $\hat{\alpha}_{max}$ are listed in table 4.1 and visualized in figure 4.8.

Method	$\hat{\alpha}_{max}$
Parameter fitting	4.894×10^{-4}
Linearization	4.013×10^{-12}
Linearization during operation	5.132×10^{-13}

Table 4.1: Step size limit estimates $\hat{\alpha}_{max}$ computed with the parameter fitting and linearization method based on random operating points and with the linearization method based on the operating points of the emergency operation example.

The step size limit estimate of the parameter fitting method is by multiple orders of magnitude higher than the step size estimates of the linearization method. During the computation of the estimates using the parameter fitting, only 24 out of the 50 random states and inputs could be used to compute the Lyapunov coefficient estimates $\hat{\gamma}$ and $\hat{\zeta}$. For the remaining 26 operating points, the coefficient estimation returns invalid values, i.e., $\hat{\gamma} \leq 0$ and/or $\hat{\zeta} \leq 0$, and therefore these operating points can not be considered in the step size limit estimation. The Lyapunov function approximation in equation (3.26) exhibits a success rate of 48% on the considered sample. Due to this and the high step size limit estimate, there is evidence, that the used approximation of the Lyapunov function does not capture all the necessary dynamics of the power system. In particular, the slow dynamics do not seem to be captured in the used combination of approximation of the Lyapunov function and random states and inputs. The step size limit α_{max} is therefore estimated too high.

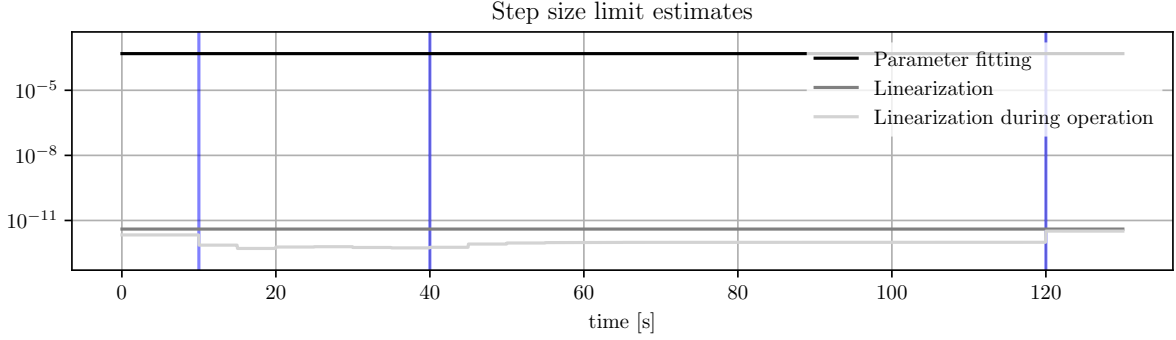


Figure 4.8: Step size limit estimate $\hat{\alpha}_{max}$ in the emergency operation set-up. The straight black and dark grey lines show the estimates based on the set of random states and inputs, while the light grey line shows how the step size limit estimate changes based on the operating points of the emergency operation simulation. The vertical blue lines mark the disconnection of line L23-24, the starting point of the controller and the reclosure of line L23-24, respectively.

Estimating the step size limit with the linearization method results in much tighter bounds on the step size. However, this method comes with downsides as well. Besides the expected missing rotor angle reference resulting in a marginally stable mode (see remark 4), at some operating points additional marginally stable modes appear. They include the states of the internal voltages of the synchronous machines, the excitation systems and the valve position of the governors. In general these modes are stable, but due to numerical issues their real parts are close enough to zero to impede the computation of a positive definite matrix $\mathbf{P}_{(i)}$, which satisfies the Lyapunov equation (3.30). Because these modes are marginally stable, they can be excluded from the Lyapunov equation with the same method used to exclude the marginally stable mode corresponding to a rotor angle reference. Besides that, the system matrix $\mathbf{A}_{(i)}$ or rather the system matrix without the marginally stable modes $\hat{\mathbf{A}}_{(i)}$, which is used in the Lyapunov equation (3.30) and needs to be inverted during the step size estimation (see equation (3.31b)), is ill-conditioned with a condition number of up to 4.31×10^{19} . This could give rise to further numerical issues, which distort the numerical value of the step size estimate.

Comparing the step size limit estimates of the linearization method based on the random states and inputs with those computed during operation with real operating points leads to additional insights. First, the random states and inputs apparently represent operating points that allow for a bigger step size limit than the initial operating point $(\mathbf{x}_0, \mathbf{w}_0)$. Therefore, the estimated step size limit during operation is lower than the linearization with the random states and inputs as long as the system is in the initial operating point ($t < 10$ s). Second, the tripping transmission line leads to a significant reduction of the step size limit estimate. Part of this reduction is due to the transient operating points, as can be seen in the time range of $10 \leq t \leq 50$ s. As other part, the change in topology, presumably the reduced meshedness, leads to a reduced step size limit estimate. This is underlined by the increase at the reclosure of the transmission line at $t = 120$ s: Although the operating point changes only very little (see figure 4.6a), the step size limit estimate increases. While the reduction due to the transients is considered in theorem 2 through the Lyapunov parameters γ and ζ and therefore is supposed to be considered in the estimates using the set of random states and inputs, the reduction due to the change in topology is not considered in theorem 2.

To verify the estimated step size limits $\hat{\alpha}_{max}$, they are tested on this simulation set-up. Since we expect a dependence of the step size limit α_{max} on the sampling time of the controller τ_{FO} and the theory used in the step size limit estimation is based on continuous time controllers, the step sizes are tested with different sampling times τ_{FO} of the controller. The small sampling

time $\tau_{FO} = 0.01$ is added to represent fast sampling without big discretization steps. Convergence of the simulation is summarized in table 4.2, where α_{lim} is the maximum step size at the corresponding sampling time for which the system converges in this set-up. For completeness, besides the computed step size limit estimates, the so far used step size $\alpha = 3 \times 10^{-5}$ is listed as well.

	τ_{FO}	
	0.01 s	5 s
4.8×10^{-4}	–	–
3.0×10^{-5}	–	✓
α 4.0×10^{-12}	✓*	✓*
5.1×10^{-13}	✓*	✓*
α_{lim}	1.0×10^{-8}	7.0×10^{-5}

Table 4.2: Convergence test for the emergency operation simulation with different step sizes α and sampling times of the FO controller τ_{FO} . α_{lim} represents the maximum step size at the given sampling time for which the system converges in this set-up.

* Theoretic convergence.

Because of the non-converging simulations with a step size of $\alpha = 4.8 \times 10^{-4}$, which corresponds to the limit estimated with the parameter fitting method, the assumption of not capturing the necessary dynamics with this method can be confirmed. Convergence of the very conservative step size limits returned by the linearization method can not be verified in simulations due to the low step size causing numerical problems. Since the step size is lower than the maximum step size corresponding to the same sampling time, convergence is guaranteed theoretically by theorem 1. These results are marked by a star (*). The linearization method seems to capture very slow dynamics, that are (at least in this example) not excited by the FO controller and lead to a very low step size limit, or is distorted by numerical issues. The results in table 4.2 further let us verify a dependence of the step size limit α_{max} on the sampling time of the discrete time controller τ_{FO} . Recent work like [34] has started exploring FO with discrete time controllers on sampled data and elaborates on its stability.

4.2.4 Robustness of Feedback Optimization Controller

Due to the feedback used in the FO controller, it is robust against some model inaccuracies. This robustness allows the FO controller to converge to a stable operating point, even if the used model information in form of the sensitivities $\nabla \mathbf{h}$ do not exactly correspond to the real steady state sensitivities. As we've seen in the economic dispatch example in section 4.2.1, inaccurate sensitivities can cause the FO controller to converge to a suboptimal operating point. This behavior has been described also in [35]. Furthermore, inaccuracies in the used sensitivities can cause increased temporary constraint violations, because the linearized expected system response used to check the output constraints in the QP (3.6) is less accurate. If the controller converges to an operating point, asymptotically all constraints will be fulfilled despite inaccurate sensitivities. However, the inaccuracies in output constraint checking can threaten stability of the system. To correct for that, the step size α can be reduced, which leads to a trade-off between designing the controller to converge as fast as possible with a step size close to the step size limit α_{max} or robust against model inaccuracies.

Besides of the mismatch in sensitivities due to model inaccuracies (like the described issue of the excitation system *SEXS*), during emergency operation a robustness against sensitivities computed based on an inaccurate topology is of interest, because the topology can change quickly and unpredictably when the power system is in emergency operation mode in case of tripping

equipment. In [14] a framework is presented to quantify model uncertainty and test the convergence of a FO controller under these uncertainties. Since in this thesis a different FO controller set-up is used (output constraints enforced by projection, see QP (3.6), whereas [14] uses penalty functions), this framework cannot be adapted to the used FO controller. To show the robustness of the FO controller against topology inaccuracies, the emergency operation example controlled by the FO controller is simulated for a set of different sensitivities. These sensitivities are based on the network topology with one missing transmission line, where for every missing transmission line a simulation is run. The resulting voltage differences between buses B23 and B24 are shown in figure 4.9.

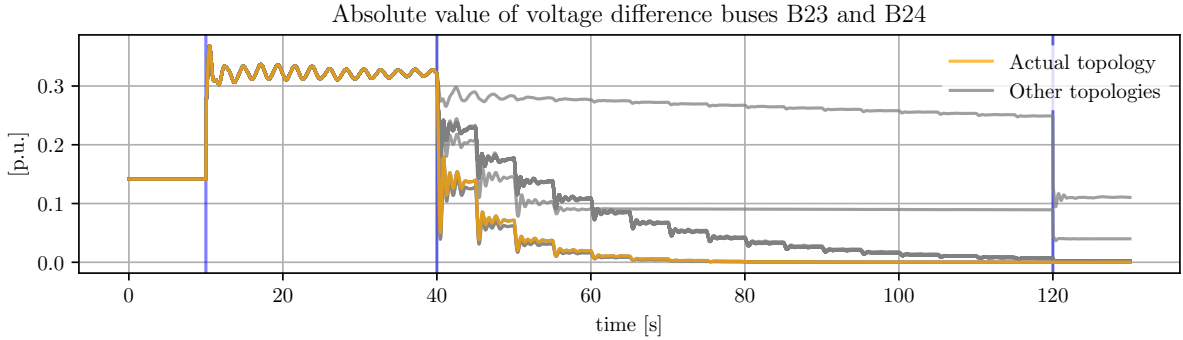


Figure 4.9: Voltage differences of buses B23 and B24 in the emergency operation simulations for the FO controller with different sensitivities. The simulation with the actual sensitivities is highlighted in orange. The vertical blue lines mark the disconnection of line L23-24, the starting point of the controller and the reclosure of line L23-24, respectively.

All sensitivities lead to a stable behavior of the FO controller. The more accurate sensitivities allow the FO controller to converge to a better operating point. This can be seen at the line highlighted in orange, which corresponds to the simulation run with sensitivities based on the actual topology. The voltage difference of one simulation shows lower results in the first 20 s of the controller ($40 \leq t \leq 60$ s). This is because inaccurate sensitivities can lead to a temporary operating point, that violates some constraints and thus reaches a lower objective value. However, this is only temporary, because the violation will be corrected.

Although there is no formal robustness guarantee, these simulation results show evidence, that the FO controller is robust against sensitivities based on a topology, which is wrong by at least one transmission line.

Chapter 5

Conclusion

A FO controller to control a power system in emergency operation mode has been implemented and tested against an OPF controller. Although the OPF controller with perfect model information should theoretically lead to optimal operating points, model inaccuracies can lead the OPF controller to suboptimal operating points and constraint violations. The FO controller, on the contrary, succeeds in controlling the power system in emergency operation mode and drives it to optimal or close to optimal operating points, where all posed constraints are fulfilled. Unfortunately, no practically useful stability certificate for the FO controller on a dynamic system could be made because of two reasons. First, the stability bound needs to be estimated, and the presented estimation methods either do not capture the necessary system dynamics and lead to too big step size limits, or capture dynamics, that are not excited by the controller, which leads to a too conservative limit. Secondly, the available theory on timescale separation does not take into account model uncertainties, which will be most likely present in a real application, especially during emergency operation of a power system. Despite the missing stability certificate, there is strong evidence that the presented FO controller is capable of controlling a power system during emergency operation and in the presence of model uncertainties. FO hence provides the necessary characteristics to facilitate emergency power system operation.

Since operational security is very important in applications like power system operation, future research is suggested in deriving certificates for stability and robustness of FO controller. The current available theory on computing the step size limit could be extended to account only for system dynamics that are excited by the controller, and thus tighten the stability limit. This might lead to a step size, which is dependent on the direction of the taken step (adjusting a voltage set point, for example, triggers different dynamics, than redispatching power). To speed up convergence of the FO controller, the step size limit further could be dependent on the current operating point. As long as the current operating point is not close to any operating limit, the step size could be increased, since there is no risk of the controller leaving the feasible region.

Appendix A

Technical Data IEEE 39 Bus System

The technical data of the IEEE 39 bus test system as used in the simulations is based on [17] and slightly adjusted to work with the changed power system models (see chapter 2) and satisfy the operating constraints \mathcal{W} defined in equation (4.1). A single line diagram of the power system is shown in figure 4.1. The system is operated at 345 kV and a nominal frequency of 60 Hz. An overview of the buses with the bus types is given in table A.2. The technical data of the transmission lines and transformers is given in tables A.3 and A.1, respectively. The parameters of the synchronous machines, the corresponding governors, excitation systems, and power system stabilizers are shown in tables A.4 - A.7. The AGC is tuned with the following parameters: $\lambda = 200$, $K_p = 0.001$, $K_i = 0.5$ and $\alpha_i = 0.1 \forall i \in [0, 10]$ (see table 2.5 for a description of these parameters).

ID	From bus	To bus	r_{ij} [Ω]	x_{ij} [Ω]	t_{ij}	t_{ji}
T2-30	B2	B30	0.000	21.544	0.976	1.000
T6-31	B6	B31	0.000	29.756	0.935	1.000
T10-32	B10	B32	0.000	23.805	0.935	1.000
T11-12	B11	B12	1.904	51.776	1.000	0.994
T13-12	B13	B12	1.904	51.776	1.000	0.994
T19-20	B19	B20	0.833	16.425	0.943	1.000
T19-33	B19	B33	0.833	16.902	0.935	1.000
T20-34	B20	B34	0.952	19.044	0.991	1.000
T22-35	B22	B35	0.000	17.021	0.976	1.000
T23-36	B23	B36	0.595	32.382	1.000	1.000
T25-37	B25	B37	0.714	27.614	0.976	1.000
T29-38	B29	B38	0.952	18.568	0.976	1.000

Table A.1: Technical data of the transformers in the IEEE 39 bus system: transformer resistance r_{ij} and reactance x_{ij} and the voltage ratios t_{ij} and t_{ji} .

ID	$v_{n,i}$ [kV]	Bus type	$p_{L,i}$ [MW]	$q_{L,i}$ [MVar]
B1	345.0	PQ		
B2	345.0	PQ		
B3	345.0	PQ	322.0	2.4
B4	345.0	PQ	500.0	184.0
B5	345.0	PQ		
B6	345.0	PQ		
B7	345.0	PQ	233.8	84.0
B8	345.0	PQ	522.0	176.0
B9	345.0	PQ		
B10	345.0	PQ		
B11	345.0	PQ		
B12	138.0	PQ	7.5	88.0
B13	345.0	PQ		
B14	345.0	PQ		
B15	345.0	PQ	320.0	153.0
B16	345.0	PQ	329.0	32.3
B17	345.0	PQ		
B18	345.0	PQ	158.0	30.0
B19	345.0	PQ		
B20	230.0	PQ	628.0	103.0
B21	345.0	PQ	274.0	115.0
B22	345.0	PQ		
B23	345.0	PQ	247.5	84.6
B24	345.0	PQ	308.6	-92.2
B25	345.0	PQ	224.0	47.2
B26	345.0	PQ	139.0	17.0
B27	345.0	PQ	281.0	75.5
B28	345.0	PQ	206.0	27.6
B29	345.0	PQ	283.5	26.9
B30	16.5	PV		
B31	16.5	Angle reference	9.2	4.6
B32	16.5	PV		
B33	16.5	PV		
B34	16.5	PV		
B35	16.5	PV		
B36	16.5	PV		
B37	16.5	PV		
B38	16.5	PV		
B39	345.0	PV	1104.0	250.0

Table A.2: Overview of the buses in the IEEE 39 bus system: Bus nominal voltage $v_{n,i}$, bus type, active and reactive load power withdrawal $p_{L,i}$ and $q_{L,i}$, respectively.

ID	From bus	To bus	Length [km]	r_{ij} [Ω/km]	x_{ij} [Ω/km]	b_{ij}^{sh} [$\mu\text{S}/\text{km}$]
L1-2	B1	B2	163.064	0.026	0.300	3.600
L1-39	B1	B39	99.188	0.012	0.300	6.353
L2-3	B2	B3	59.909	0.026	0.300	3.607
L2-25	B2	B25	34.121	0.244	0.300	3.595
L3-4	B3	B4	84.508	0.018	0.300	2.201
L3-18	B3	B18	52.768	0.025	0.300	3.404
L4-5	B4	B5	50.784	0.019	0.300	2.220
L4-14	B4	B14	51.181	0.019	0.300	2.269
L5-6	B5	B6	10.316	0.023	0.300	3.535
L5-8	B5	B8	44.436	0.021	0.300	2.791
L6-7	B6	B7	36.501	0.020	0.300	2.601
L6-11	B6	B11	32.534	0.026	0.300	3.587
L7-8	B7	B8	18.251	0.026	0.300	3.591
L8-9	B8	B9	144.020	0.019	0.300	2.219
L9-39	B9	B39	99.188	0.012	0.300	10.165
L10-11	B10	B11	17.060	0.028	0.300	3.590
L10-13	B10	B13	17.060	0.028	0.300	3.590
L13-14	B13	B14	40.072	0.027	0.300	3.613
L14-15	B14	B15	86.095	0.025	0.300	3.572
L15-16	B15	B16	37.295	0.029	0.300	3.852
L16-17	B16	B17	35.311	0.024	0.300	3.193
L16-19	B16	B19	77.366	0.025	0.300	3.301
L16-21	B16	B21	53.561	0.018	0.300	3.997
L16-24	B16	B24	23.408	0.015	0.300	2.441
L17-18	B17	B18	32.534	0.026	0.300	3.406
L17-27	B17	B27	68.638	0.023	0.300	3.937
L21-22	B21	B22	55.545	0.017	0.300	3.880
L22-23	B22	B23	38.088	0.019	0.300	4.072
L23-24	B23	B24	138.863	0.019	0.300	2.184
L25-26	B25	B26	128.150	0.030	0.300	3.363
L26-27	B26	B27	58.322	0.029	0.300	3.452
L26-28	B26	B28	188.060	0.027	0.300	3.486
L26-29	B26	B29	247.969	0.027	0.300	3.486
L28-29	B28	B29	59.909	0.028	0.300	3.492

Table A.3: Technical data of the lines in the IEEE 39 bus system: line resistance r_{ij} and reactance x_{ij} and the shunt susceptance of the line b_{ij}^{sh} along with the line length.

ID	bus	S_i [MW]	$p_{set,i}$ [p.u.]	$v_{set,i}$ [p.u.]	H [s]	D	X_d [p.u.]	X_q [p.u.]	X'_d [p.u.]	X'_q [p.u.]	X''_d [p.u.]	X''_q [p.u.]	T'_{d0} [s]	T'_{q0} [s]	T''_{d0} [s]	T''_{q0} [s]
G1	B39	10 000	0.100	1.030	5.000	0	2.000	1.900	0.600	0.800	0.400	0.400	7.000	0.700	0.050	0.035
G2	B31	700	0.000	0.982	4.329	0	2.065	1.974	0.488	1.190	0.350	0.350	6.560	1.500	0.050	0.035
G3	B32	800	0.813	0.983	4.475	0	1.996	1.896	0.425	0.701	0.360	0.360	5.700	1.500	0.050	0.035
G4	B33	800	0.790	0.997	3.575	0	2.096	2.064	0.349	1.328	0.280	0.280	5.690	1.500	0.050	0.035
G5	B34	300	0.680	1.012	4.333	0	2.010	1.860	0.396	0.498	0.267	0.267	5.400	0.440	0.050	0.035
G6	B35	800	0.813	1.049	4.350	0	2.032	1.928	0.400	0.651	0.320	0.320	7.300	0.400	0.050	0.035
G7	B36	700	0.800	1.064	3.771	0	2.065	2.044	0.343	1.302	0.308	0.308	5.660	1.500	0.050	0.035
G8	B37	700	0.771	1.028	3.471	0	2.030	1.960	0.399	0.638	0.315	0.315	6.700	0.410	0.050	0.035
G9	B38	1 000	0.830	1.027	3.450	0	2.106	2.050	0.570	0.587	0.450	0.450	4.790	1.960	0.050	0.035
G10	B30	1 000	0.300	1.048	4.200	0	1.000	0.690	0.310	0.690	0.250	0.250	10.200	1	0.050	0.035

Table A.4: Technical data of the synchronous machines in the IEEE 39 bus system as described in table 2.1 and the power rating of the synchronous machines S_i . The armature winding resistance of the synchronous machines is neglected in the used simulation set-ups.

ID	Unit	R	D_t	V_{min}	V_{max}	T_1 [s]	T_2 [s]	T_3 [s]
GOV1	G1	0.050	0	0	1.000	0.200	1.000	2.000
GOV2	G2	0.050	0	0	1.000	0.200	1.000	2.000
GOV3	G3	0.050	0	0	1.000	0.200	1.000	2.000
GOV4	G4	0.050	0	0	1.000	0.200	1.000	2.000
GOV5	G5	0.050	0	0	1.000	0.200	1.000	2.000
GOV6	G6	0.050	0	0	1.000	0.200	1.000	2.000
GOV7	G7	0.050	0	0	1.000	0.200	1.000	2.000
GOV8	G8	0.050	0	0	1.000	0.200	1.000	2.000
GOV9	G9	0.050	0	0	1.000	0.200	1.000	2.000
GOV10	G10	0.050	0	0	1.000	0.200	1.000	2.000

Table A.5: Technical data of the governors in the IEEE 39 bus system, as described in table 2.2.

ID	Unit	K	T_a [s]	T_b [s]	T_c [s]	E_{min} [p.u.]	E_{max} [p.u.]
AVR1	G1	100.000	2.000	10.000	0.500	-3.000	3.000
AVR2	G2	100.000	2.000	10.000	0.500	-3.000	3.000
AVR3	G3	100.000	2.000	10.000	0.500	-3.000	3.000
AVR4	G4	100.000	2.000	10.000	0.500	-3.000	3.000
AVR5	G5	100.000	2.000	10.000	0.500	-3.000	3.000
AVR6	G6	100.000	2.000	10.000	0.500	-3.000	3.000
AVR7	G7	100.000	2.000	10.000	0.500	-3.000	3.000
AVR8	G8	100.000	2.000	10.000	0.500	-3.000	3.000
AVR9	G9	100.000	2.000	10.000	0.500	-3.000	3.000
AVR10	G10	100.000	2.000	10.000	0.500	-3.000	3.000

Table A.6: Technical data of the excitation systems in the IEEE 39 bus system, as described in table 2.3.

ID	Unit	K	T [s]	T_1 [s]	T_2 [s]	T_3 [s]	T_4 [s]	H_{lim} [p.u.]
PSS1	G1	50.000	10.000	0.500	0.500	0.050	0.050	0.030
PSS2	G2	50.000	10.000	0.500	0.500	0.050	0.050	0.030
PSS3	G3	50.000	10.000	0.500	0.500	0.050	0.050	0.030
PSS4	G4	50.000	10.000	0.500	0.500	0.050	0.050	0.030
PSS5	G5	50.000	10.000	0.500	0.500	0.050	0.050	0.030
PSS6	G6	50.000	10.000	0.500	0.500	0.050	0.050	0.030
PSS7	G7	50.000	10.000	0.500	0.500	0.050	0.050	0.030
PSS8	G8	50.000	10.000	0.500	0.500	0.050	0.050	0.030
PSS9	G9	50.000	10.000	0.500	0.500	0.050	0.050	0.030
PSS10	G10	50.000	10.000	0.500	0.500	0.050	0.050	0.030

Table A.7: Technical data of the power system stabilizers in the IEEE 39 bus system, as described in table 2.4.

Bibliography

- [1] European Court of Auditors. “Wind and solar power for electricity generation: significant action needed if EU targets to be met”. In: *Special Report No 08/2019: Wind and solar power for electricity generation* (2019).
- [2] Philipp Felber. “So knapp entging die Schweiz einem Blackout”. In: *Tagesanzeiger* (May 2019). <https://www.tagesanzeiger.ch/story/20957737>.
- [3] N. K. Roy and H. R. Pota. “Current Status and Issues of Concern for the Integration of Distributed Generation Into Electricity Networks”. In: *IEEE Systems Journal* 9.3 (2015), pp. 933–944.
- [4] Allen J. Wood, Bruce F. Wollenberg, and Gerald B. Sheblé. *Power Generation, Operation, and Control*. 3rd ed. New York: John Wiley & Sons, 2013.
- [5] Hassan Haes Alhelou et al. “A Survey on Power System Blackout and Cascading Events: Research Motivations and Challenges”. In: *Energies* 12.4 (2019).
- [6] ENTSO-E. *Special Protection Schemes*. ENTSO-E SG SPD Report. Brussels, 2012.
- [7] Jan Machowski. *Power system dynamics: stability and control*. Wiley, 2008.
- [8] Mary B. Cain and Richard P. O’Neill. “History of Optimal Power Flow and Formulations”. In: 2012.
- [9] Lingwen Gan and Steven H. Low. “An Online Gradient Algorithm for Optimal Power Flow on Radial Networks”. In: *IEEE Journal on Selected Areas in Communications* 34.3 (2016), pp. 625–638.
- [10] Adrian Hauswirth et al. “Online optimization in closed loop on the power flow manifold”. In: *2017 IEEE Manchester PowerTech*. 2017, pp. 1–6.
- [11] Emiliano Dall’Anese and Andrea Simonetto. “Optimal Power Flow Pursuit”. In: *IEEE Transactions on Smart Grid* 9.2 (2018), pp. 942–952.
- [12] Adrian Hauswirth et al. *Optimization Algorithms as Robust Feedback Controllers*. 2021.
- [13] Adrian Hauswirth et al. “Timescale Separation in Autonomous Optimization”. In: *IEEE Transactions on Automatic Control* 66.2 (Feb. 2021), pp. 611–624.
- [14] Marcello Colombino, John W. Simpson-Porco, and Andrey Bernstein. “Towards robustness guarantees for feedback-based optimization”. In: *2019 IEEE 58th Conference on Decision and Control (CDC)*. 2019, pp. 6207–6214.
- [15] Sairaj V. Dhople et al. “Reexamining the Distributed Slack Bus”. In: *IEEE Transactions on Power Systems* 35.6 (2020), pp. 4870–4879.
- [16] Hallvar Haugdal and Kjetil Uhlen. *An Open Source Power System Simulator in Python for Efficient Prototyping of WAMPAC Applications*. 2021.
- [17] *GitHub Repository: DynPSSimPy*. github.com/hallvar-h/DynPSSimPy. Accessed: June 2021. Mar. 2021.

- [18] Bikash Paland and Balarko Chaudhuri. *Robust Control in Power Systems*. Kluwer Academic Publishers, 2005.
- [19] Hallvar Haugdal, Norwegian university of science and technology, personal communication. Aug. 2021.
- [20] ENTSO-E. *Documentation on Controller Tests in Test Grid Configurations*. ENTSO-E SG SPD Report. Brussels, 2013.
- [21] Petros Aristidou, Davide Fabozzi, and Thierry Van Cutsem. “Dynamic Simulation of Large-Scale Power Systems Using a Parallel Schur-Complement-Based Decomposition Method”. In: *IEEE Transactions on Parallel and Distributed Systems* 25.10 (2014), pp. 2561–2570.
- [22] Petros Aristidou. *PyRAMSES*. <https://pyramses.paristidou.info>. Accessed: July 2021. Mar. 2021.
- [23] Markus Mirz et al. “DPsim – A dynamic phasor real-time simulator for power systems”. In: *SoftwareX* 10 (2019), p. 100253.
- [24] Verena Häberle et al. “Non-Convex Feedback Optimization With Input and Output Constraints”. In: *IEEE Control Systems Letters* 5.1 (2021), pp. 343–348.
- [25] J.W. Chinneck. *Feasibility and Infeasibility in Optimization: Algorithms and Computational Methods*. International Series in Operations Research & Management Science. Springer, 2007.
- [26] Andreas Wächter and Lorenz T. Biegler. “On the implementation of an interior-point filter line-search algorithm for large-scale nonlinear programming”. In: *Mathematical Programming* 106.1 (Apr. 2005), pp. 25–57.
- [27] Yoshiaki Kawajir et al. *Introduction to Ipopt: A tutorial for downloading, installing, and using Ipopt*. Apr. 2015.
- [28] James R. Munkres. *Analysis On Manifolds*. 1st ed. Advanced Books Classics. CRC Press, 2018.
- [29] Saverio Bolognani and Florian Dörfler. “Fast power system analysis via implicit linearization of the power flow manifold”. In: *2015 53rd Annual Allerton Conference on Communication, Control, and Computing (Allerton)*. 2015, pp. 402–409.
- [30] Wilson J. Rugh. *Linear System Theory*. 2nd ed. Prentice-Hall, Inc., 1996.
- [31] Thomas M. Athay, Robin Podmore, and Sudhir Virmani. “A Practical Method for the Direct Analysis of Transient Stability”. In: *IEEE Transactions on Power Apparatus and Systems* 98.2 (1979), pp. 573–584.
- [32] Edgar Gómez et al. “Independent Estimation of Generator Clustering and Islanding Conditions in Power System with Microgrid and Inverter-Based Generation”. In: *Wide Area Power Systems Stability, Protection, and Security*. Springer International Publishing, 2021, pp. 523–553.
- [33] Joel A. E. Andersson et al. “CasADi – A software framework for nonlinear optimization and optimal control”. In: *Mathematical Programming Computation* 11.1 (2019), pp. 1–36.
- [34] Giuseppe Belgioioso et al. *Sampled-Data Online Feedback Equilibrium Seeking: Stability and Tracking*. Sept. 2021.
- [35] Lukas Ortmann et al. “Experimental validation of feedback optimization in power distribution grids”. In: *Electric Power Systems Research* 189 (Dec. 2020), p. 106782.